

Master's Thesis

Characterization, Modeling and Performance Prediction of an Electric Microfluidic Cell Manipulation Device

Carried out for the purpose of obtaining the degree of Master of Science, submitted at
Vienna University of Technology, Faculty of Electrical Engineering and Information
Technology.

By

Jan Pilsinger

Under the supervision of

Mag. rer. nat. Klemens J. Wassermann

Molecular Diagnostics, Center for Health & Bioresources, AIT Austrian Institute
of Technology GmbH

&

Ao.Univ.Prof. Dipl.-Ing. Dr.techn. Eugenijus Kaniusas

Institute of Electrodynamics, Microwave and Circuit Engineering, E354

Affidavit

I hereby declare that this work has been prepared in accordance with the Code of Conduct - Rules for the Securing of Good Scientific Practice (in the current version of the respective information sheet of the Vienna University of Technology), in particular without the inadmissible assistance of third parties and without the use of aids other than those indicated. The data and concepts taken directly or indirectly from other sources are marked with indication of the source.

The work has not been presented in the same or similar form in other examination procedures, either at national or international level.

Eidesstattliche Erklärung

Hiermit erkläre ich, dass die vorliegende Arbeit gemäß dem Code of Conduct - Regeln zur Sicherung guter wissenschaftlicher Praxis (in der aktuellen Fassung des jeweiligen Mitteilungsblattes der TU Wien), insbesondere ohne unzulässige Hilfe Dritter und ohne Benutzung anderer als der angegebenen Hilfsmittel, angefertigt wurde. Die aus anderen Quellen direkt oder indirekt übernommenen Daten und Konzepte sind unter Angabe der Quelle gekennzeichnet.

Die Arbeit wurde bisher weder im In- noch im Ausland in gleicher oder in ähnlicher Form in anderen Prüfungsverfahren vorgelegt.

Contents

1	Abstract	1
1.1	English Version	1
1.2	German Version	2
1.3	Aim	3
2	Introduction	4
2.1	Theoretical Foundation	4
2.1.1	Electroporation - The concept of temporary pores	4
2.1.2	The Electrode-Electrolyte Interface	8
2.1.3	Schottky Diode with an N-Type Semiconductor	10
2.2	Modeling of Electrochemical Systems	11
2.2.1	Non-Ideal Circuit Elements: CPE & Warburg Impedance	12
2.2.2	Randles Circuit & Coated Metal Modell	13
3	Materials and Methods	16
3.1	Materials	16
3.1.1	Instruments	16
3.1.2	Disposables	17
3.1.3	Prototype materials	17
3.1.4	Media and Supplements	18
3.1.5	Software	18
3.2	Methods	19
3.2.1	Electrode and Prototype generation - Pipette Design	19
3.2.2	Schottky Diode Sample Preparation	19
3.2.3	Diode Characteristics Measurement	20
3.2.4	EIS Measurement	21
3.2.5	Electrical Potential Progression in an Electrolyte - The "Bath" Setup	22
4	Results and Discussion	24
4.1	Titanium Oxide Coating	24
4.2	Electrical Impedance Spectroscopy	25
4.2.1	Electrolyte	25
4.2.2	Bode & Nyquist Plots	26
4.3	Electrical determination of System elements	29
4.3.1	Diode Characteristic	29
4.3.2	Electrode Bath Experiments	34
4.4	Equivalent Circuit	46
4.4.1	First Approach	46
4.4.2	Coating Model	49
4.4.3	Results	50
4.5	Equivalent Circuit Simulation	53

4.5.1	Implementation and Simulation Setup	53
4.5.2	Transient Potential Drops over System Elements	55
4.6	Statistical Lysis Model	59
4.6.1	Data Pooling Strategy	59
4.6.2	Derived Features and Augmentation	61
4.6.3	Data Exploration	62
4.6.4	Multinomial Logistic Regression Model	63
4.6.5	Model Performance	65
4.6.6	Cell Lysis Threshold Voltage / Electric Field Strength	67
5	Conclusion	72
5.1	Outlook	73
	References	74

1 Abstract

1.1 English Version

Reliable and accurate methods for cell and tissue manipulation are fundamental for a wide range of scientific and commercial endeavors. Progress in this field is quickly reflected in sectors such as pharmaceuticals, biotechnology or health care and yields substantial social benefits.

AIT Austrian Institute of Technology develops a novel microfluidic electrode concept for cell specific lysis and transfection, the so-called "Electrical Cell Manipulation Device" (ECMD). The ECMD produces finely dosed electric fields in the kV/cm range, at voltages of only 10-40 V. These strong electric fields cause a transient formation of pores in the cell membrane (permeabilization), which can be used for cell specific lysis as well as for the transport of active substances or plasmids into the cells, i.e. transfection.

The system consists of two plane-parallel titanium electrodes passivated with a high- κ dielectric. This passivation of thermally oxidized titanium leads to a decoupling of the target area from galvanic currents and frees the biological targets from unwanted electrochemical reactions. Otherwise, these lead to material detachment, bubble formation or changes in the pH-value. This countermeasure prevents the impairment or even destruction of markers or decomposition of samples, as well as unspecific side effects on cells.

In order to better understand the system and optimize the process parameters, detailed electrotechnical modeling and quantification is required. The aim of this master's thesis is therefore to characterize the ECMD electrotechnically and to shed light on the essential (bio)physical processes.

Furthermore, a model is created which is to provide conclusions on the actual effective internal field strength in dependence on conventional parameters such as voltage amplitude, frequency, waveform etc. In particular, an equivalent circuit diagram is derived which is based on the evaluation of extensive electrical impedance spectroscopy and is then simulated in PSpice®. In the final step, the findings and a comprehensive set of data from biological experiments are combined in the derivation of a statistical model in MATLAB®, which allows for predictions of the lysis rate under specification of all methodological parameters.

The application of electric fields to biological samples promises high potential in the fields of biotechnology and medicine. During this thesis, the foundation was laid for a deeper understanding of the ECMD and the transient electric field strength within the electrolyte. These results may initiate further innovation by providing new input for better designs. Furthermore, the compiled prediction model may be extended to incorporate lysis rate predictions for different cell types and thus allow researchers or medical staff to conveniently eliminate arbitrary subsets of cells from a sample suspension.

1.2 German Version

Verlässliche und akkurate Methoden zur Zell- und Gewebemanipulation sind für verschiedenste wissenschaftliche und kommerzielle Unterfangen von hoher Bedeutung. Fortschritte in diesem Bereich schlagen sich rasch in Branchen wie der Pharmazie, Biotechnologie oder dem Gesundheitswesen nieder und bringen hohen gesellschaftlichen Nutzen.

Das AIT Austrian Institute of Technology entwickelt ein neuartiges mikrofluidisches Elektrodenkonzept zur zellspezifischen Lyse und Transfektion, das sogenannte "Electrical Cell Manipulation Device" (ECMD). Das ECMD produziert fein dosierbare elektrische Felder im kV/cm-Bereich, bei angelegten Spannungen von lediglich 10-40 V. Diese starken elektrischen Felder bewirken eine vorübergehende Ausbildung von Poren in der Zellmembran (Permeabilisierung), welche zur zellspezifischen Lyse ungewollter Organismen sowie zum Transport von Wirkstoffen oder Plasmiden in die Zellen verwendet werden kann, z.B. Transfektion.

Das System besteht aus zwei planparallelen Titanelektroden, die mit einem High- κ -Dielektrikum passiviert sind. Diese Passivierung aus thermisch oxidiertem Titanoxid führt zu einer Entkopplung des Zielraumes von galvanischen Strömen und befreit die biologischen Ziele von unerwünschten elektrochemischen Reaktionen. Diese führen ansonsten zu Materialablösung, Blasenbildung oder Änderungen des pH-Wertes. Unselektiven Nebeneffekten sowie der Beeinträchtigung oder gar Zerstörung von Markern oder Proben wird dadurch vorgebeugt.

Um das System besser zu verstehen und die Prozessparameter zu optimieren bedarf es einer detaillierten elektrotechnischen Modellierung und Quantisierung. Es soll deshalb das Ziel dieser Masterarbeit sein, das ECMD elektrotechnisch zu charakterisieren und die wesentlichen (bio)physikalischen Prozesse zu beleuchten.

Des weiteren wird ein Modell gebildet, welches Rückschlüsse auf die tatsächlich wirksame innere Feldstärke in Abhängigkeit konventioneller Parameter wie Spannungsamplitude, Frequenz, Kurvenform etc. gibt. Im Speziellen wird dafür ein Ersatzschaltbild abgeleitet, welches auf der Auswertung umfangreicher elektrischer Impedanzspektroskopien basiert und anschließend in PSpice[®] simuliert wird. Im letzten Schritt vereinigen sich die gewonnenen Erkenntnisse sowie ein umfangreicher Datensatz aus biologischen Experimenten in der Herleitung eines statistischen Modells in MATLAB[®], welches Voraussagen über die Lyserate unter Angabe aller methodischen Parameter ermöglicht.

Die Anwendung von elektrischen Feldern auf biologische Proben birgt ein hohes Potenzial in den Bereichen Biotechnologie und Medizin. Während dieser Arbeit wurde der Grundstein für ein tieferes Verständnis des ECMD und der transienten elektrischen Feldstärke innerhalb des Elektrolyten gelegt. Diese Ergebnisse können neue Impulse für bessere Designs liefern. Darüber hinaus kann das zusammengestellte Prädiktionsmodell erweitert werden, um beispielsweise Vorhersagen für verschiedene Zelltypen zu integrieren, so dass Forscher oder medizinisches Personal beliebige Teilmengen von Zellen bequem aus einer Probensuspension entfernen können.

1.3 Aim

The aim of this Master's Thesis was to elucidate the internal working principles of the above mentioned Electrical Cell Manipulation Device (ECMD).

For this purpose, firstly, extensive electrical analysis of system elements was conducted by means of impedance spectroscopy and manual measurements. An indication for internal transient field strength within the electrolyte was extracted. The acquired data was merged to derive a model for the ECMD in the form of a fitted equivalent circuit. Subsequently, state variables like powers, currents and peak voltages have been extracted by simulation runs with varying process parameters.

Finally, the acquired information was combined with extensive data on lysis experiments, leading to a predictive statistical model to forecast lysis rates in dependence on parameters like applied voltage, exposure time, frequency or cell type. The validation of this model was conducted by comparison of predicted lysis rates with previous experiments.

2 Introduction

The terms *electroporation* or *electropermeabilization* are used to describe the manipulation of cells or tissue by application of a strong electric field. Use-cases for this technology are manifold. For example, it can be used to deliver cargo into the intracellular space to which the cell is impermeable under regular conditions, such as certain drugs or plasmids. Another application is the cell specific lysis due to certain biophysical characteristics of different cell types[27].

The basic idea of the electroporation technique can be traced back to the 70s of the last century[28]. Nowadays, it gains new momentum, since the enormous progress of miniaturization made by the semi-conductor industry as well as improvements in understanding and designing microfluidic systems open up huge future potential in microbiological and biomedical research circles.

Despite the diversity of tools commercially available to the modern scientist, such as accurate and miniaturized electronic components or computer aided pattern recognition, modeling and automation, a highly multivariate set of hurdles has yet to be overcome. This technology is still held back by a lack of understanding the underlying biophysical dependencies and the complex electrode-electrolyte interactions. Experimental setups open up multiple degrees of freedom - to state but a few, the electric field alone has numerous parameters which need to be examined and optimized, such as field strength, frequency, curve form or field distribution - not to mention the substantial (statistical) variance introduced by working with biological samples. Overcoming these aforementioned obstacles and consequently mastering, for example, the cell-specific lysis process, promises accuracy gains and cost reductions in healthcare technologies, including, but not limited to, molecular diagnostics applications.

In the following, I provide a brief review of a common biophysical model for electroporation and adjacent physical processes, that are relevant to the application-oriented scientist. Furthermore, I introduce the basic approach for modeling an electrochemical system by means of an equivalent circuit. Such a model has to represent charge carrier mobility, hydroelectric effects, such as double layers or electrode potentials and other time-dependent behaviour, that can be introduced by diffusion, for instance. For this purpose, a comprehensive set of relevant circuit elements is reviewed.

2.1 Theoretical Foundation

2.1.1 Electroporation - The concept of temporary pores

If living cells are subjected to an electrical field, a number of interaction processes take place. Most of them involve the membrane of the cells as central points of action. The cell membrane consists of a phospholipid bilayer, which has two electrically relevant features. Firstly, it acts as a good insulator due to its high resistance. Secondly, it yields

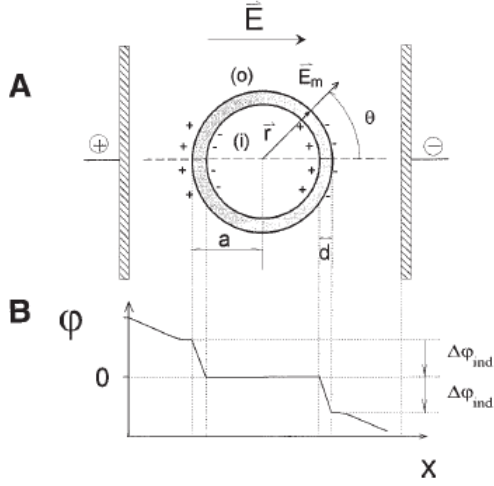


Figure 1: Cellular cross-membrane potential and electric polarization. (A) A spherical membrane of radius a with a membrane thickness d is subjected to an external electric field E . (B) shows the electrical potential profile ϕ across the cell membranes. The drop in the induced membrane potential in the direction of E is marked as $\Delta\phi_{ind}$. Taken from [28].

strong capacitive behaviour. This is due to its small thickness of approximately 7 to 10 nm[1], compared to the cell diameter, which is usually several orders of magnitude larger: take, for example, an erythrocyte disk diameter of 6.2 - 8.2 μm [2]. In contrast to a conventional capacitor, the charge carriers are not electrons but solvated ions like sodium, potassium and calcium, surrounded by their respective hydration shells. An applied voltage across the cell leads to an accumulation of ions of opposite charge at the membrane, enhancing the potential gradient within the bilayer, as illustrated in figure 1.

Additionally, the cells themselves uphold a physiologic potential difference between the intra- and extracellular space, the so-called *resting potential*. This potential can be described by the famous “Goldman-Hodgkin-Katz Constant Field equation”, or simply the “Goldman equation”[5]:

$$V_m \cong -60\text{mV} \log_{10} \frac{P_K[K]_{in} + P_{Na}[Na]_{in} + P_{Cl}[Cl]_{out}}{P_K[K]_{out} + P_{Na}[Na]_{out} + P_{Cl}[Cl]_{in}} \quad (2.1)$$

with V_m as the actual potential difference across the membrane and P_i as the respective permeability in (cm/s) for the ions sodium, potassium and chlorine. V_m depends highly on the cell type - for example, erythrocytes show a resting potential of only -8.4 mV[6], while a “[...] typical bacterial membrane potential is around -150 mV”[7].

The geometrical dimensions of cells, which often can be approximated as spheres, influence the local electric field distribution of an applied homogeneous electric field. Due to differing permittivities within the phospholipid bilayer relative to water, as well as variable electric conductivities between the intra- and extracellular space, we examine a concentration of electric flux through the cell membrane. The resulting induced trans-membrane potential depends on the relative angle in respect to the field vector \vec{E} . This

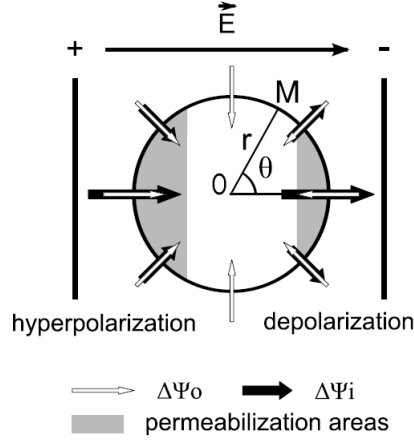


Figure 2: Schematic of the transmembrane potential of a cell subjected to an external homogeneous electric field. Resulting asymmetric potential distribution due to the superposition of the physiologic resting potential $\Delta\Psi_0$ and the induced potential $\Delta\Psi_i$, indicated by overlapping field strength arrows. Taken from [8].

relation can be described by the steady state Schwan equation[3][4]

$$\Delta\varphi_m = 1.5 ER \cos \theta \quad (2.2)$$

or the more general first order Schwan equation for the description of transient membrane potentials during the first microseconds resulting from a DC pulse[3][4]

$$\Delta\varphi_m = 1.5 ER \cos \theta (1 - e^{-\frac{t}{\tau_m}}) \quad (2.3)$$

with E as the external electric field, R as the cell radius, θ as the angle measured from the cell center relative to the field orientation and t as time. τ_m represents the characteristic time constant of the charging membrane

$$\tau_m = \frac{R\epsilon_m}{2d\frac{\sigma_i\sigma_e}{\sigma_i+2\sigma_e} + R\sigma_m} \quad (2.4)$$

with σ_i, e, m standing for the cytoplasmic, external and membrane conductivity and ϵ_m as the dielectric permittivity of the membrane. d takes the membrane thickness into account. The superposition of the induced potential and the cell's resting potential leads to a hyperpolarization and depolarization region at the "poles" of the cell. Figure 2 provides an illustration of the angle-dependent transmembrane potential $\Delta\varphi_m(\theta)$ and the de-/hyperpolarization effect.

The resulting electric field strength depends strongly on the geometrical composition of the specimen. The induced electric field strength can be written as $E_{\text{ind}} = -\Delta\varphi_{\text{ind}}/d$. Subsequently, assuming a spherical geometry, we arrive at the local field strength

$$E_{\text{ind}} = \frac{3R}{2d} E f(\sigma_m) \cos \theta \quad (2.5)$$

with R as cell radius, d as membrane thickness and a conductivity factor $f(\sigma_m)$ [28]. The field amplification factor $(3R)/(2d)$ can grow particularly large for large vesicles

and cells. For example, with a cell radius of $10\text{ }\mu\text{m}$ and a membrane thickness of 5 nm , this factor becomes 3×10^3 [28]. To a cell membrane, which can be regarded more as a thin layer of liquid than a rigid construct, held together mostly by surface tension and hydrophobicity, this can have drastic effects.

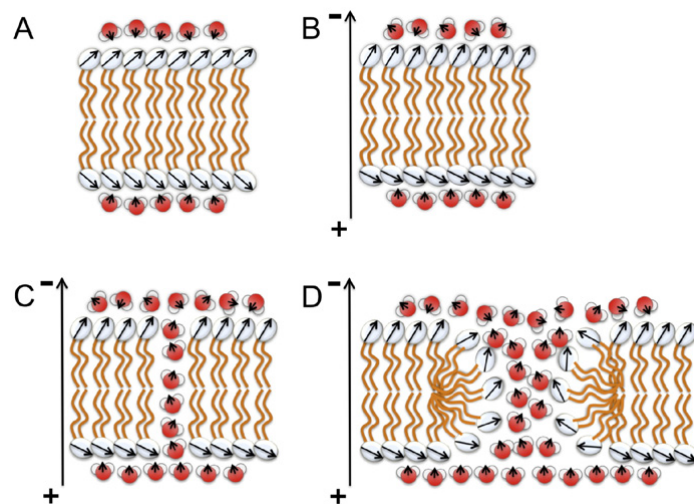


Figure 3: A) In absence of an external field interfacial water dipoles preferentially point to the hydrophobic core of the membrane partially shielding the phospholipid headgroup dipoles. B) The application of an external electric field results in a reinforced alignment of water dipoles at the cathodic membrane leaflet and a weakened orientation at the anodic side. Also the lipid headgroups slightly tilt according to the field direction. C) The modified energetics of the membrane increases the probability of the formation of a closed water wire across the membrane. D) The intrusion of water into the membrane hydrophobic core lowers the barrier for lipid protrusions towards the membrane center and finally results in the formation of a metastable hydrophilic membrane pore. Taken from [25].

The building unit of the phospholipid bilayer is the phospholipid. By nature, it is a polar molecule and is therefore very sensitive to an electric field, within which it will reorient itself to reach a state of lower energy. The resulting moment of force destabilizes the bilayer and, at some point, the forces are strong enough to disrupt the membrane locally. The cell, however, will not instantaneously burst like a balloon. Instead, the probability of the formation of a closed water wire across the membrane is increased. If such a water intrusion occurs, the hydrophobic phospholipid tails inside the membrane core will reorient themselves to reach a new energetic minimum. Consequently, a metastable hydrophilic membrane pore is established[25]. This process of deliberate disturbance is called *formation of transient pores* and is illustrated in figure 3.

The pore model was introduced after the observation of penetrations of small ions and

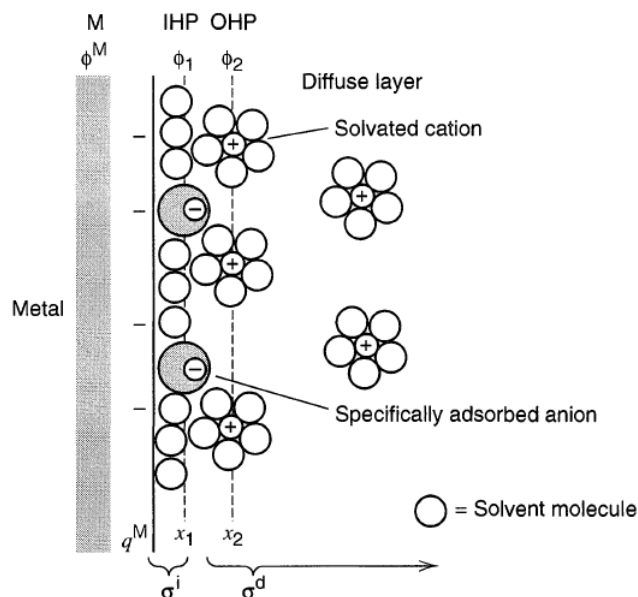


Figure 4: Double layer model considering specifically adsorbed ions. Inner Helmholtz Plane IHP, Outer Helmholtz Plane OHP, charge of IHP σ_i , charge of the diffuse layer σ_d , spatial distances $x_{1,2}$. Taken from [10].

ionic drug-like dyes long after the application of field pulses. The typical duration of an applied voltage pulse is within the microsecond to millisecond range. However, diffusion effects can be observed even seconds after poration, eliminating the intuitive mechanism of mere electro-motive forces "pulling" ionic cargo into cells.

2.1.2 The Electrode-Electrolyte Interface

The *electrochemical double layer* is the phase boundary between an electron conductor (the electrode) and an ion conductor (the electrolyte). Typically there are two charge layers at the phase boundary in the charged state, which - as in any capacitor - have the opposite sign. The "thickness" of the charged layers, i.e. the mean extent perpendicular to the surface, is approximately 0.1 to 10 nm. It is described by the Debye length and depends on the mobility and the concentration of the ions.

Using the example of the Graham Model, I will provide a brief introduction to the current understanding of electrode-electrolyte-interface.

The solution side of a charged electrode-electrolyte interface can be imagined to consist of several layers. The layer closest to the electrode is called *inner Helmholtz plane* (IHP), after Hermann von Helmholtz, who was the first to explicitly describe the double layer at electrode-electrolyte interfaces in 1879 (see [9]). This charged layer consist of ions in direct contact to the electrode. Those ions are also called *specifically adsorbed* [10]. The charged electrode and the IHP form the Helmholtz Double Layer, which poses the simplest model for charged electrode-electrolyte interfaces. However, the Helmholtz model does not encompass other important factors, such as diffusion or mixing of different ions

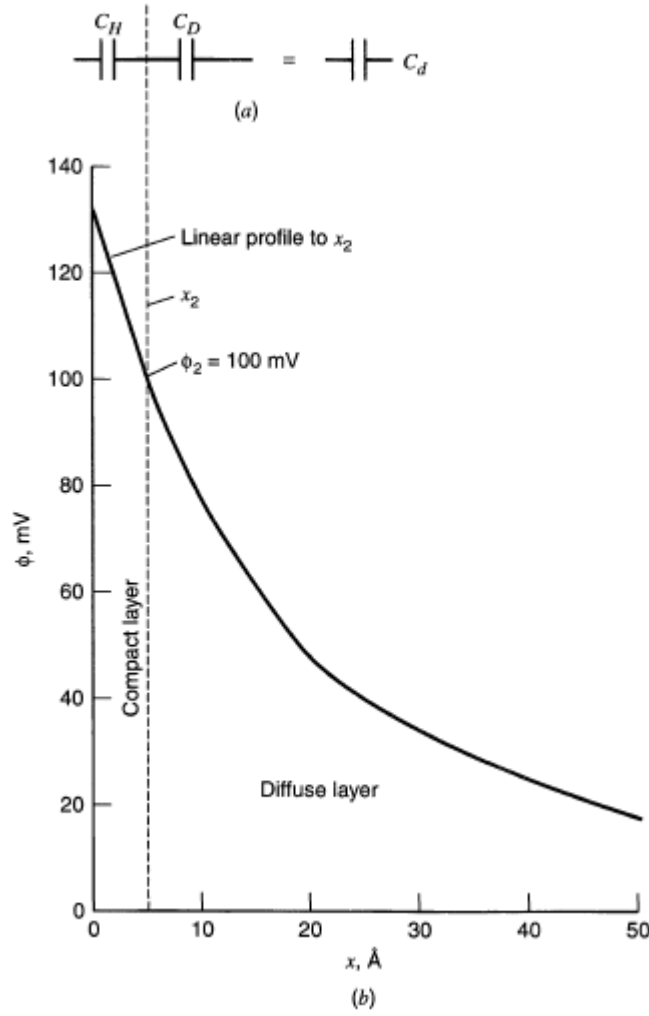


Figure 5: (a) A series network of Helmholtz-layer and diffuse-layer capacitances in the GCS model. (b) Resulting potential profile through the solution side, calculated for a concentration of 10^{-2} M 1:1 electrolyte in water at 25°C . Taken from [10].

in the solution.

Therefore, another theory was introduced in 1910 by Loius G. Gouy and 1913 by David L. Chapman. The idea was to introduce an ion layer, which is composed of solvated ions with their respective hydration shells - water molecules, that form an envelope around the ion due to the dipole character of water and electrostatic attraction. This hydration shell forms a lower boundary for the distance x_2 between the metal and solvated ions. These ions are called *nonspecifically adsorbed* and "[...] the locus of centers of these nearest solvated ions is called the *outer Helmholtz plane* (OHP)" [10]. Figure 4 elucidates the IHP, OHP as well as the diffuse layer.

Furthermore, these ions form the so-called *diffuse layer*, which extends far from the OHP into the electrolyte and represents a significant improvement to the Helmholtz model. As a result, the charge distribution can be interpreted as a function of the distance from

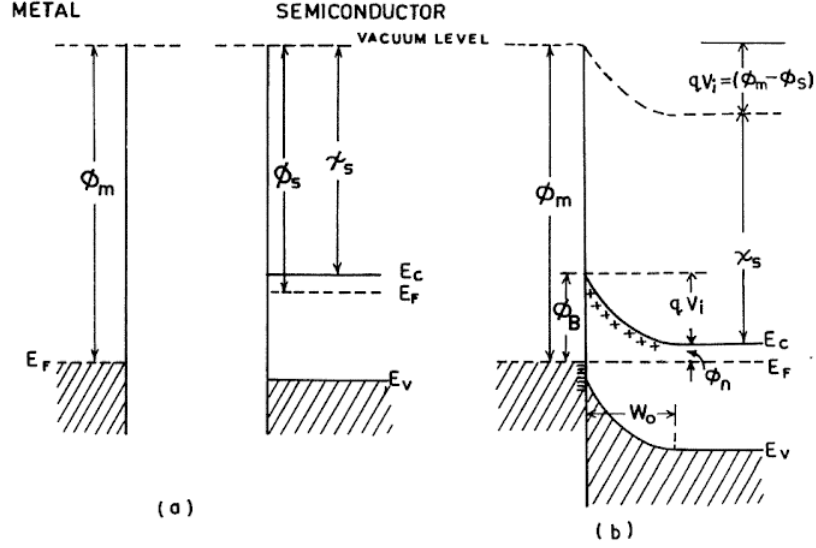


Figure 6: Electron energy band diagrams of metal contact to n-type semiconductor with $\phi_m > \phi_s$. (a) Neutral materials separated from each other and (b) thermal equilibrium situation after the contact was made. Taken from [13].

the metal surface, which decreases exponentially from the surface to the liquid. Figure 5 illustrates the potential profile in the Gouy-Chapman-Stern (GCS) model.

2.1.3 Schottky Diode with an N-Type Semiconductor

A Schottky diode is a special diode in electronics that does not have a p-n junction (semiconductor-semiconductor junction) but a (blocking) metal-semiconductor junction. This interface between metal and semiconductor is called a Schottky contact or, based on the potential barrier that occurs, a Schottky barrier. Like the p-n junction, the Schottky diode is a rectifier. With Schottky diodes, the material composition (e.g. doping of the semiconductor) is selected such that a depletion zone forms in the interface in the semiconductor. Thus, the nonlinear Schottky contact differs from metal-semiconductor transitions under other conditions, such as the ohmic contact, which shows the behavior of a partially linear ohmic resistance.

The function of a Schottky diode with n-doped semiconductor material can be explained using the electron band model. Assuming that the metal's work function $q * \phi_m$ is greater than the electron affinity of the semiconductor $q * \chi$, a potential stage of height $qV_i = (\phi_m - \phi_s)$ will be created at the interface between the Fermi energy W_F of the metal and the bottom edge of a semiconductor conduction band. Figure 6 illustrates this relation.

As a result, electrons will move towards the metal, until the Fermi energies of both

materials are aligned. The electrons accumulate as a surface charge at the interface, creating a depletion zone of opposite charge in the semiconductor, whose width is "[...] appreciable because the donor concentration in the semiconductor is several orders of magnitude smaller than the electron concentration in the metal"[13].

If a positive voltage is applied (negative pole on the n-type semiconductor), electrons are forced into the depletion zone and the potential barrier becomes smaller. Electrons can then flow from the semiconductor into the metal ("forward bias"). On the other hand, if a negative voltage is applied, electrons are driven away from the metal and the thickness of the depletion zone increases ("reverse bias"). Only a very small current occurs because a few electrons of the metal can overcome the barrier by thermal excitation or tunnel through. However, if the voltage in the blocking direction is too high, a breakthrough occurs.

Not all metal-semiconductor interfaces form a Schottky diode - it is also possible for an ohmic contact to be established. This is the case, if the working energy of the metal is smaller than the working energy of an n-type semiconductor, $\varphi_m < \varphi_s$. If close contact is established, electrons flow from the metal into the semiconductor, creating a negative space charge region, while leaving a positive surface charge at the metal surface. As a result, no depletion zone is created, as the electrons are the majority charge carriers, thus establishing a non-rectifying ohmic contact[13].

The above-mentioned explanations speak of an n-type semiconductor, which creates a rectifying metal-semiconductor contact (Schottky Diode), if $\varphi_m > \varphi_s$ and an ohmic contact, if $\varphi_m < \varphi_s$. The opposite is true for a p-type semiconductor[13].

2.2 Modeling of Electrochemical Systems

There are numerous methods for modeling electrochemical systems - we will focus on representations by equivalent circuits.

Information about an electro(chemical) system can be conveniently gathered by conducting an electrical impedance spectroscopy (EIS). As a result, individual characteristics of a system can be visualized by a Bode or Nyquist plot and subsequently, an equivalent circuit can be fitted to the data. The structure and composition of the resulting circuit can give quantified information about the underlying physical, chemical and electrical phenomena. However, while convenient, this method of abstracting a system to purely electrical terms also poses a risk of misguidance, since the most adapted equivalent circuit does not necessarily represent physical meaning. Therefore, this approach is best used, when an intuitive understanding of the system is already established and an initial narrowing in of known circuit structures can be done[16].

A number of system properties can be emulated by ideal circuit elements. For example, the resistance of an electrolyte can be modeled as a resistor. The other ideal circuit elements at our disposal are capacitors and inductors. Yet, some processes can only be

reproduced by so-called *distributed EC elements*[14], such as the constant phase element (CPE) (often used for double layer phenomena) and the Warburg diffusion impedance. Table 1 provides an overview of ideal circuit elements used for modeling.

Component	Equivalent Element	Current vs. Voltage	Impedance
Resistor	$R \ (\Omega)$	$V = IR$	R
Capacitor	$C \ (\text{F, or } \Omega^{-1}s)$	$I = C \, dV/dt$	$1/j\omega C$
Inductor	$L \ (\text{H, or } \Omega s)$	$V = L \, dI/dt$	$j\omega L$
Infinite diffusion	$Z_W \ (\Omega)$		$R_W/\sqrt{j\omega}$
CPE	$Q \ (\Omega^{-1}s^\alpha)$		$1/Q(j\omega)^\alpha$

Table 1: Summary of circuit elements used in EC models and their respective impedance. Taken from [14].

2.2.1 Non-Ideal Circuit Elements: CPE & Warburg Impedance

Usually, real systems show some deviation from theoretical, ideal behaviour. In electrochemical setups, the resulting electrical current is a superposition of several distributed microscopic phenomena. This leads to frequency dependent impedances, which are difficult to model. Structural causes for deviations from ideal capacitor and resistor responses can be for example[14][11]:

- electrode inhomogeneity and surface roughness (3D)
- electrode porosity (3D)
- variability in thickness and conductivity of surface coating (3D)
- slow, uneven adsorption process (2D)
- nonuniform potential and current distribution at the surface (2D)
- grain boundaries and crystal phases on polycrystalline electrode (2D)

A good approach to summarize a number of these "disorders" in one circuit element is the *constant phase element* (CPE). Its name is derived by the fact, that the phase angle of such an element is AC-frequency independent. The CPE impedance can be written as[11]:

$$Z_{\text{CPE}} = \frac{1}{Q(j\omega)^\alpha} = \frac{1}{Q\omega^\alpha} [\cos(\alpha\pi/2) - j \sin(\alpha\pi/2)] \quad (2.6)$$

with Z_{CPE} being the impedance of the constant phase element, the effective CPE coefficients $Q \ (\Omega^{-1}s^\alpha)$ and $\alpha = [0...1]$ as well as the circular frequency $\omega \ (\text{s}^{-1})$. This expression converges towards an ideal capacitor for $\alpha = 1$ and towards a resistor for $\alpha = 0$ [14]. Many distributed processes exist, where the exponent α lies between 0.4

and 0.6. In these cases, one can think of this EC element to represent a kind of "leaky capacitive" behaviour.

It must be noted, that the CPE is popular for modeling the double layer capacitance, since the double layer often shows a distributed CPE-like behaviour, instead of that of a pure capacitor. "Several theories have been proposed to account for the nonideal behavior of the double layer, but none has been universally accepted. As a first approximation, one can treat α as an empirical constant"[14]. All the while, as pointed out in section 2.2, caution has to be taken, since the CPE has great potential to fit arbitrary impedance spectra, simply by adapting the α -parameter. Furthermore, the behaviour of a CPE has also been reported to be caused by resistivity distributions in films[15]. In this publication, B. Hirschorn et al. simulated the impedance of a material with a normal power-law distribution of local resistivity and showed consistency with the CPE. Apart from that, their approach may "potentially be applied approximately for semiconducting materials"[15].

Another noteworthy non-ideal circuit element is the *Warburg Diffusion Impedance*. It is used to describe diffusion processes or phenomena in general, where mass transfer is relevant. If the electrochemical cell is large compared to the diffusion length, we speak of semi-infinite diffusion[17]. In this case, the CPE transforms into the Warburg impedance with $\alpha = 0.5$ and $Q = 1/R_W$, resulting in

$$Z_W = R_W / \sqrt{j\omega} \quad (2.7)$$

with Z_W as Warburg Impedance and R_W as diffusion resistance[14]. The Warburg element can also be used to model diffusion processes with spatial boundary conditions, which is then called finite diffusion. If the diffusion species are reflected from the electrodes (totally blocked), the impedance transforms to

$$Z_W = R_D \coth(\sqrt{(j\omega L_D^2)/D}) / \sqrt{(j\omega L_D^2)/D} \quad (2.8)$$

with D as diffusion coefficient of the species and L_D as thickness of the diffusion layer. If they are instantly consumed at the electrode,

$$Z_W = R_D \tanh(\sqrt{(j\omega L_D^2)/D}) / \sqrt{(j\omega L_D^2)/D} \quad (2.9)$$

applies[14].

2.2.2 Randles Circuit & Coated Metal Modell

The *Randles Circuit*, as depicted in figure 7, is a fundamental equivalent circuit used to model electrochemical reactions at flat electrode-electrolyte interfaces in presence of semi-infinite linear diffusion of electroactive species. It consists of a bulk solution resistance in series with a parallel circuit, that encompasses a Warburg impedance in

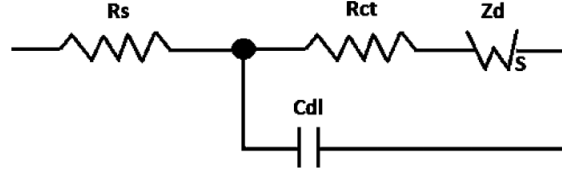


Figure 7: The ideal Randles circuit consists of the double layer capacitance C_{dl} , the Warburg diffusion impedance Z_d , a charge transfer resistance R_{ct} and the solution resistance R_s . Taken from [19].

series with a charge transfer resistance, that describes the "electrode reaction" [18] and a double layer capacity. It was first introduced by John Randles in 1947 [18].

Today, it is used in a broad range of applications as a starting point for investigating electrical impedance spectra, such as for examinations of polyoxometalate layer-by-layer films [19], modeling the steel-concrete interface [20] or quantifying performance losses in polymer electrolyte fuel cells [21].

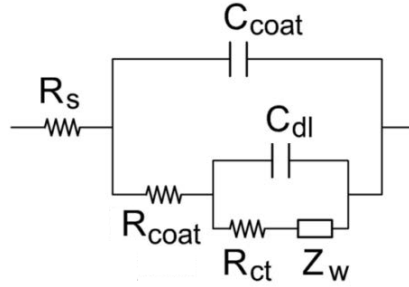


Figure 8: The coated metal model consists of a solution resistance R_s , a coating capacity C_{coat} , resistance associated with the coating R_{coat} , double layer capacitance C_{dl} , charge transfer resistance R_{ct} and a Warburg diffusion impedance Z_w . Taken and modified from [22].

The Randles circuit is also the basis for the *coated metal model*. Therein, electrode reactions, which are often mapped onto the charge transfer resistance R_{ct} , are sometimes neglected and a coating resistance and capacitance are introduced. Figure 8 illustrates the model.

As visible in figure 8, it is an extended Randles circuit, nested in a parallel circuit representing the coating. Depending on the specific experimental setup or material under examination, there are different interpretations of the coating resistance R_{coat} . For example, in a study of electrodeposited epoxy coatings it is interpreted as "[...] the coating pore resistance due to diffusion of electrolyte" [22], while Duval et al. see "[...] ionic transport through the coating representing its flaws. A flaw could consist of a weak area of coating, or a crack extending through the coating." [23]. One can conclude,

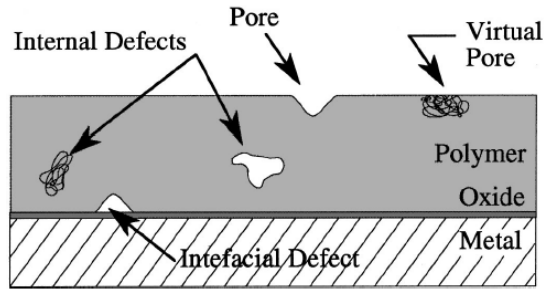


Figure 9: Schematic of a polymere-coated metal. Taken from [24].

that R_{coat} takes into account irregularities of the coating, such as small cracks, pores or internal and interfacial defects (see figure 9).

3 Materials and Methods

3.1 Materials

3.1.1 Instruments

- Metrohm / Eco Chemie Autolab PGSTAT30 Potentiostat / Galvanostat
- Arium[®] pro UV ultrapure water system (Sartorius AG)
- Centrifuge 5430 (Eppendorf AG) with rotors
 - F-35-6-30 (Eppendorf AG)
 - FA-45-30-11 (Eppendorf AG)
- Certoclave CV-EL 12L/18L autoclave steam steriliser (Certoclav Sterilizer GmbH)
- Inverted microscope CKX41 (Olympus corporation) with
 - Objectives (Olympus corporation)
 - * Plan 4X – for brightfield observation
 - * CACHN10XPhP – for phase contrast observation
 - * LCAchN20XPhP – for phase contrast observation
 - * LCAchN40XPhP – for phase contrast observation
 - Phase contrast slider IX2-SLP (Olympus corporation)
 - X-cite[®] 120Q wide field fluorescence microscope excitation light source (Excelitas Technologies corporation)
 - Prosilica GT 1920C camera (Allied Vision)
 - Fluorescence excitation mirrors (Olympus corporation) with information in dichroic mirror, excitation filter, barrier filter and application in brackets:
 - * B-excitation (DM500, BP460-490C, BA520IF; e.g. for FITC imaging)
 - * G-excitation (DM570, BP480-550C, BA590; e.g. for PI imaging)
 - * U-excitation (DM400, BP360-370, BA420; e.g. for Hoechst imaging)
- Herasafe[™] KS, Class II Biological Safety Cabinet (Thermo Fisher Scientific Inc.)
- Heracell[™] VIOS 160i CO₂ incubator (Thermo Fisher Scientific Inc.)
- Function / Arbitrary Waveform Generator DG4102 (Rigol Technologies Inc.)
- Voltage amplifier WMA-300 (Falco Systems BV)

- Digital Oscilloscope DS1104B (Rigol Technologies Inc.)
- Rigol DP832 Programmable DC Power Supply (Rigol Technologies Inc.)
- True RMS Multimeter Fluke 287 (Fluke Corporation)
- SUB Aqua Pro water bath SAP12 (Grant Instruments Ltd)
- mLINE[®] and Proline[®] Plus micropipettes (Sartorius AG)
 - 0.5 - 10 μl (Ref.: 725020 and 728020)
 - 2 - 20 μl (Ref.: 725030 and 725030)
 - 10 - 100 μl (Ref.: 725050 and 728050)
 - 20 - 200 μl (Ref.: 725060 and 728060)
 - 100 - 1000 μl (Ref.: 725070 and 728070)
- Nabertherm L 9/11/SKM/P330 muffle furnace (Schaefer & Lehmann GmbH)

3.1.2 Disposables

- CELLSTAR[®] cell culture flasks 175 cm^2 , red standard (Greiner Bio One International GmbH, Ref.: 660160)
- Falcon[®] tissue culture flasks 75 cm^2 , blue vented cap (Corning Inc., Ref.: 353136)
- G3692 Acheson Silver DAG 1415 with brush
- SafeSeal SurPhob filter tips (Biozym)
 - 10 μl (Ref.: VT0200)
 - 20 μl (Ref.: VT0220)
 - 100 μl (Ref.: VT0230)
 - 200 μl (Ref.: VT0240)
 - 1250 μl (Ref.: VT0270)
- 50 ml self-standing centrifuge tubes (Corning Inc., Ref.: 430921)
- 15 ml CELLSTAR[®] centrifuge tubes (Greiner Bio One International GmbH, Ref.: 188271)

3.1.3 Prototype materials

- 0.005" (110 μm) grade 2 titanium foil sheets (Titanium Goat)

- 81 μm ARcare[®] 90445 clear polyester double-sided adhesive tape (Adhesive Research, Inc., Ref.: 90445)

3.1.4 Media and Supplements

- RPMI medium 1640 (Gibco, Life Technologies, Ref.: 21875-034)
- Anti-Anti antibiotic antimycotic 100x (Gibco, Life Technologies, Ref.: 15240-096)
- Fetal bovine serum (FBS) (Thermo Fisher Scientific Inc., Ref.: 10500)

3.1.5 Software

- Graphpad Prism[®] 7
- Matlab[®] R2013b & R2017b
- NOVA[®] 1.11
- OrCAD Capture CIS[®] Lite
- PSpice AD[®] Lite
- ImageJ[®] 1.5
- Microsoft Excel[®] 2010 & 2013

3.2 Methods

3.2.1 Electrode and Prototype generation - Pipette Design

The pipette electrodes are based on a sandwich design with a succession of titanium, titanium oxide and polymer layers.

In the first step, commercially pure titanium sheets (grade 2) with a thickness of 110 μm are cut into rectangles of approximately 1.5 cm x 3.5 cm. Thereafter, the sheets are cleaned in an ultrasonic bath of acetone, isopropanol and ultrapure water for twenty minutes. After drying with compressed air, they are placed in a muffle furnace on titanium spacers. The oxidation layer is produced by thermal oxidation, which is achieved by subjecting the samples to a 650°C environment for three hours with a two-hour ramp time. Subsequently, the oxidized titanium sheets are passively cooled for twenty hours in the muffle furnace.

In order to permit good electrical contact, part of the oxide layer is (manually) removed with a diamond file until a surface resistance below 10 Ω is measured using a conventional multimeter. We choose the sheet's bottom side, which was in direct contact with the spacers during oxidation and is therefore irregularly coated. The side with the uniform oxide layer is used for the microfluidic field chamber.

The microfluidic field chamber is created by applying double sided adhesive tape with a thickness of 81 μm . Two stripes are aligned with the long edges, leaving a gap of approximately 2 mm in the center of the titanium sheet. Thereafter, a second titanium sheet is attached on top, complementing the sandwich design. The bare electrode contacts should be on the outer top and bottom sides.

Finally, the tip of a 20 μl pipette tip is removed and the resulting open cone glued to the construct with self-curing adhesive. Attention has to be given to leak-tightness and avoidance of obstructions. The electrode system is tested by filling the microfluidic field chamber with phosphate buffered saline (PBS) and applying a square wave voltage signal of 10-30 V at a frequency of 100 Hz. The resulting current characteristics are measured on an oscilloscope. If the current exhibits solely capacitive behaviour, the prototype is considered functional.

3.2.2 Schottky Diode Sample Preparation

Titanium oxide is an n-type semiconductor and forms a Schottky diode with the underlying pure titanium substrate.

In order to attain a measurable sample for extraction of the diode characteristic, an oxidized titanium sheet was covered with a layer of silver conductive paste with an area of 1 cm^2 . After one hour of drying, another layer is applied, this time fixating a small part of pared wire which will function as an electrical contact. The sample is left to

dry for another hour and subsequently a third layer of silver paste is laid on in order to increase stability.

The second electrical contact is created by filing off the oxide layer with a diamond file. In order to avoid surface currents, this has to be done at a location sufficiently far away from the coated area or on the other side of the titanium sheet. The circuit can be closed by means of alligator clips.

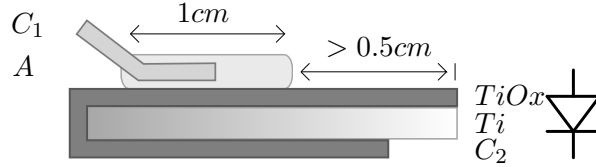


Figure 10: Electrical contact with the oxide layer surface is established by a 0.5 mm wire which is integrated in adhesive silver paste.

C_1	Contact 1 - 0.5 mm wire
C_2	Contact 2 - area of exposed titanium
A	Adhesive layer of silver paste
$TiOx$	Titanium oxide layer
Ti	Titanium core

3.2.3 Diode Characteristics Measurement

A diode characteristic inherent in titanium oxide and titanium is theoretically predicted. However, the specific parameters, such as forward bias, forward voltage drop, leakage current and reverse breakdown voltage, had yet to be examined for the custom thermally oxidized titanium used in our setup.

As testing sample we used a twofold contacted Ti-TiOx-Ag sheet as described in section 3.2.2. The experimental setup consisted of a series connection of sample, a Rigol DP832 Programmable DC Power Supply (Rigol Technologies Inc.) and a True RMS Multimeter Fluke 287 (Fluke Corporation). The power supply was used as a direct voltage source and the multimeter as amperemeter.

The applied voltage was incremented in 0.1 mV steps, starting at 0 V and commencing in the reverse bias region until a significant increase in reverse current was measured. Subsequently, the forward region was examined in the same manner. If possible, a voltage range of -5 V to 3 V was covered.

In order to avoid destructive current breakthroughs in the forward as well as the reverse bias regions, a current limit of 50 mA was essential. However, the measured current

remained highly volatile. In order to obtain usable and reasonable results nonetheless, the multimeter was configured to calculate the measurand's mean in real time. For each respective data point, the mean was calculated over 3 seconds before notation and the applied voltage switched off immediately to avoid heating effects.

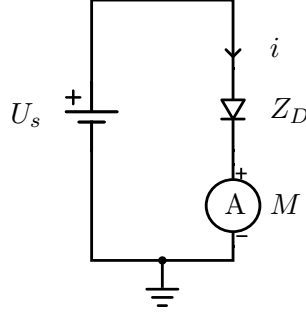


Figure 11: Equivalent circuit for the diode characteristic extraction.

U_s	DC programmable power source
i	Current, $i \in [-50...50]$ mA
Z_D	Oxidized titanium electrode sample sheet
M	Multimeter for current measurement

3.2.4 EIS Measurement

The Electrical Impedance Spectroscopies (EIS) of the Electrical Cell Manipulation Device (ECMD) were conducted by means of Autolab PGSTAT30 Potentiostat/Galvanostat and NOVA 1.11 Software. Both the traditional ECMD design and the pipette design were examined. A voltage amplitude of 10 mV was applied in a frequency range of 0.1 Hz to 1 MHz. Fourty Data points were acquired with a waiting time of five seconds separating every impedance measurement. Examination samples consisted of the electrode prototypes containing four different solutions respectively, studied in order of increasing conductivity:

- Ultra-pure water - conductivity $3 \mu\text{S}/\text{cm}$
- Sucrose solution - conductivity $6 \mu\text{S}/\text{cm}$
- Sucrose/PBS mixture - conductivity $167 \mu\text{S}/\text{cm}$
- PBS (resting and flowing) - conductivity $16 \mu\text{S}/\text{cm}$

Before every bulk solution swap, the entire field chamber of the ECMD was flushed one time with the solution to be measured subsequently.

3.2.5 Electrical Potential Progression in an Electrolyte - The "Bath" Setup

Although there are several mathematical models available, which describe the spatial electrical potential in a fluid, it is difficult to make predictions about the interaction between a diode and a solution when a certain voltage is applied.

In our case, an additional layer of complexity is added. Our oxidized titanium electrode shows diode-like behaviour, which means that its resistance depends on the voltage drop across the oxide layer. This voltage drop, however, depends not only on the applied voltage, but also on the ion distribution within the liquid, which in turn depends on the voltage drop over the diode (since liquid and diode form a classic voltage divider). What is more, the ion distribution changes transiently due to an electromotive force on the ions and counteracting diffusion, until a dynamic equilibrium is eventually established.

In order to measure the hydro-electro-dynamic effect of a semiconductor used as passivation on the solution, the following experimental setup was implemented. To gain information on the transient electric field strength within our prototype, we recreate the sandwich design (two passivated electrodes facing each other, separated by an electrolyte). In contrast to the standard distance of $81\mu m$, we use $1cm$, creating a bath setup, in which there is space to position two electrode probes.

An illustration of the measurement setup is provided in figure 12:

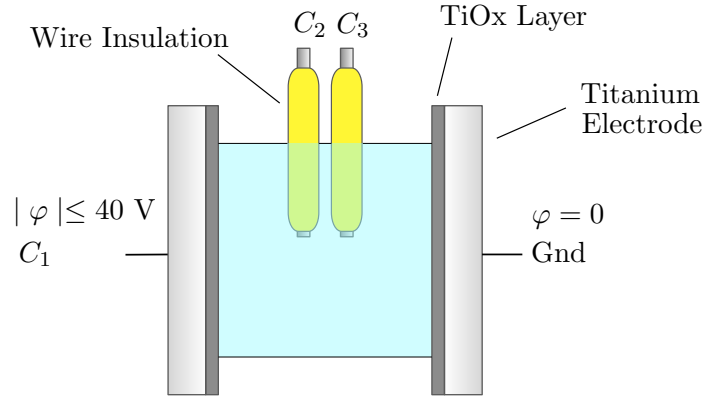


Figure 12: Experimental setup for measuring time-resolved internal electric potentials.

C_1	Channel 1, voltage application point
$C_{2,3}$	Channels 2 and 3 for measurement
φ	Electric potential

Similar to the common 4-point probes method, these electrode probes, fixed at a defined and constant distance, are connected to Channel 2 and 3 of an oscilloscope with an internal impedance of $10\text{ M}\Omega$ and sense the potential at their respective spatial position

relative to the ground potential. Since the internal impedance of the oscilloscope is very high in comparison to all resistances within the examined circuit, miscurrents over the probe electrodes can be neglected and their influence on the intrafluidic electric field considered small.

As a result, a range of high-resolution time-resolved signals can be recorded and are available for post processing, to assess time constants or potential drops between elements, for example.

4 Results and Discussion

4.1 Titanium Oxide Coating

The titanium electrodes are coated with a 600-800 nm high- κ -dielectric passivation layer[27] created by thermal oxidation. The resulting titanium oxide coating serves as a barrier between electrolyte and titanium, suppressing electrochemical reactions and therefore guaranteeing a benign environment for living specimen in the intra-electrode space.

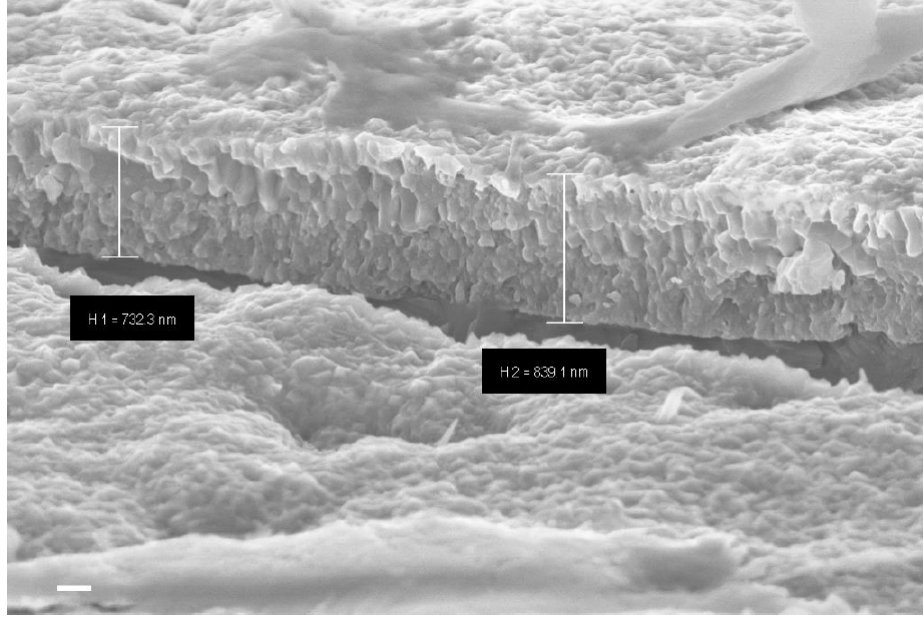


Figure 13: SEM images of the titanium oxide layer. The coating thickness in this example lies between 730 and 840 nm. Size bar: 200 nm. H1 = 732.3 nm, H2 = 839.1 nm. Taken from [29].

The coating can be expected to introduce a certain capacitance and resistance to the system. However, due to its roughness and small defects, such as cracks and pores, as well as the individual thermal oxidation process, its capacity and resistance are hard to assess upfront. Therefore, it can only be modeled as a distributed component. A good model and its theoretical foundation can be found in sections 2.2.2 and 4.4.2.

Besides its function as a coating, another effect is added: due to oxygen vacancies, titanium oxide is an intrinsic n-type semiconductor[26]. If brought into close contact with a conductor, a Schottky diode may be formed. As a result, diode-like behaviour is observed - see sections 2.1.3, 4.3.1 and 4.3.2.

4.2 Electrical Impedance Spectroscopy

Several electric impedance spectroscopies (EIS) have been performed on the established ECMD prototype as well as on the pipette design. The following electrolytes (depicted in table 3) have been tested over a frequency range of 0.1 Hz to 1 MHz:

Type	Conductivity ($\mu\text{S}/\text{cm}$)
Pure water (MilliQu)	3
Sucrose solution	6
Sucrose + PBS	167
PBS	1600
flowing PBS	1600

Table 2: By means of EIS examined solutions for both the ECMD and Pipette Prototype.

4.2.1 Electrolyte

As already mentioned in section 4.2.2, the electrolyte can be reliably assigned. According to the well-known relation between conductivity and resistance

$$R = \frac{l}{\gamma A} \quad (4.1)$$

with the resistance R , conductivity γ , length of electric path l and conductor cross section A , we get the following values, depicted in table 3, for the respective bulk resistances.

Type	Conductivity	Measured R	Theoretical R
Pure water (MilliQu)	3 $\mu\text{S}/\text{cm}$	2.228 k Ω	2.7 k Ω
Sucrose solution	6 $\mu\text{S}/\text{cm}$	1.133 k Ω	1.35 k Ω
Sucrose + PBS	167 $\mu\text{S}/\text{cm}$	59.2 Ω	48.5 Ω
PBS	1.6 mS/cm	5.87 Ω	5.06 k Ω

Table 3: Comparison between theoretical and measured values for bulk resistance. The theoretical calculation is based on a conductor cross section area of $A = 1 \text{ cm}^2$, conductor length $l = 81 \text{ }\mu\text{m}$ and the respective given electrolyte conductivity.

The measured values have been extracted by using interpolant splines or shape-preserving interpolation (norm of residuals = 0) for graph smoothing, since few data points are available at the relevant frequency range.

Due to the manual production process of the prototypes, a deviation from theoretical values is to be expected. This concerns both the distance between titanium sheets l and the cross section area A . In this light, a deviation of R from theoretical values of up to 22% (Sucrose + PBS) seems justifiable.

Furthermore, several electrolytic layer effects need to be considered. At the electrode-electrolyte interface, we have firstly the Helmholtz double layer, which induces capacitive behaviour, and secondly the diffusion layer, which dominates at low frequencies. Both are distributed phenomena and therefore show strongly frequency-dependent behaviour. Further elucidations can be found in section 2.1.2.

4.2.2 Bode & Nyquist Plots

The results of the EIS measurements were visualized via Matlab R2013b[®] and are depicted in the following Bode and Nyquist diagrams.

At first glance, the Bode diagram reveals a system with two time constants. The cut-off frequencies are shifted to higher values in accordance with an increasing conductivity of the bulk solution. Those frequencies roughly divide the graphs into three areas. For example, ultra pure water, with a conductivity of $3 \mu\text{S}/\text{cm}$, shows slightly non-linear capacitive behaviour in a frequency range below $5 \cdot 10^2 \text{ Hz}$ with tremendous impedance values up to $1\text{-}2 \text{ M}\Omega$, followed by an ohmic plateau that stretches to approximately $5 \cdot 10^4 \text{ Hz}$ and an eventual capacitive descend in impedance.

The phase shift emphasizes the non-linear area in the low-frequency range by showing a shift of $50^\circ\text{-}60^\circ$, instead of 90° in a purely capacitive system. We see a local maximum at 2 Hz for ultra pure water or $[1\text{-}2] \cdot 10^3 \text{ Hz}$ for PBS, indicating a dominating capacitive component at this point. The ohmic plateau is re-emphasized by a local phase shift minimum, followed by an ascend to nearly 90° in the very high frequency range of 10^6 Hz .

The low frequency range capacitive behaviour implies a kind of slow displacement current. Effects with ions as charge carriers seem promising, since their kinematics are defined mainly by inertia and their finite mobility within the electrolyte. Options include therefore for example polarization of the electrolyte by ionic movement (α -dispersion) and diffusion effects.

The ohmic plateau can be explained for all EIS samples by the solution conductivity and geometrical considerations.

The subsequent capacitive descend might origin from (dis)charging double layer(s) at the electrode-electrolyte interface, or simply from the geometrical capacitance of the sandwich design.

When examining the Nyquist plot in figure 15, two noticeable peculiarities strike the eye. Firstly, at low impedances, which account for high frequencies, a pronounced semi-circle is visible, which shows no signs of depression. From an electrotechnical perspective, this is a clear indicator for the occurrence of an RC-circuit with an ideal capacitor[14]. In electrochemical setups, this implies a charge transfer resistance in an electro-chemical reaction. However, the passivation layer should be chemically inactive. Furthermore, the circles diameter (Z' -axis) favorably fit the bulk solution resistances. This is another

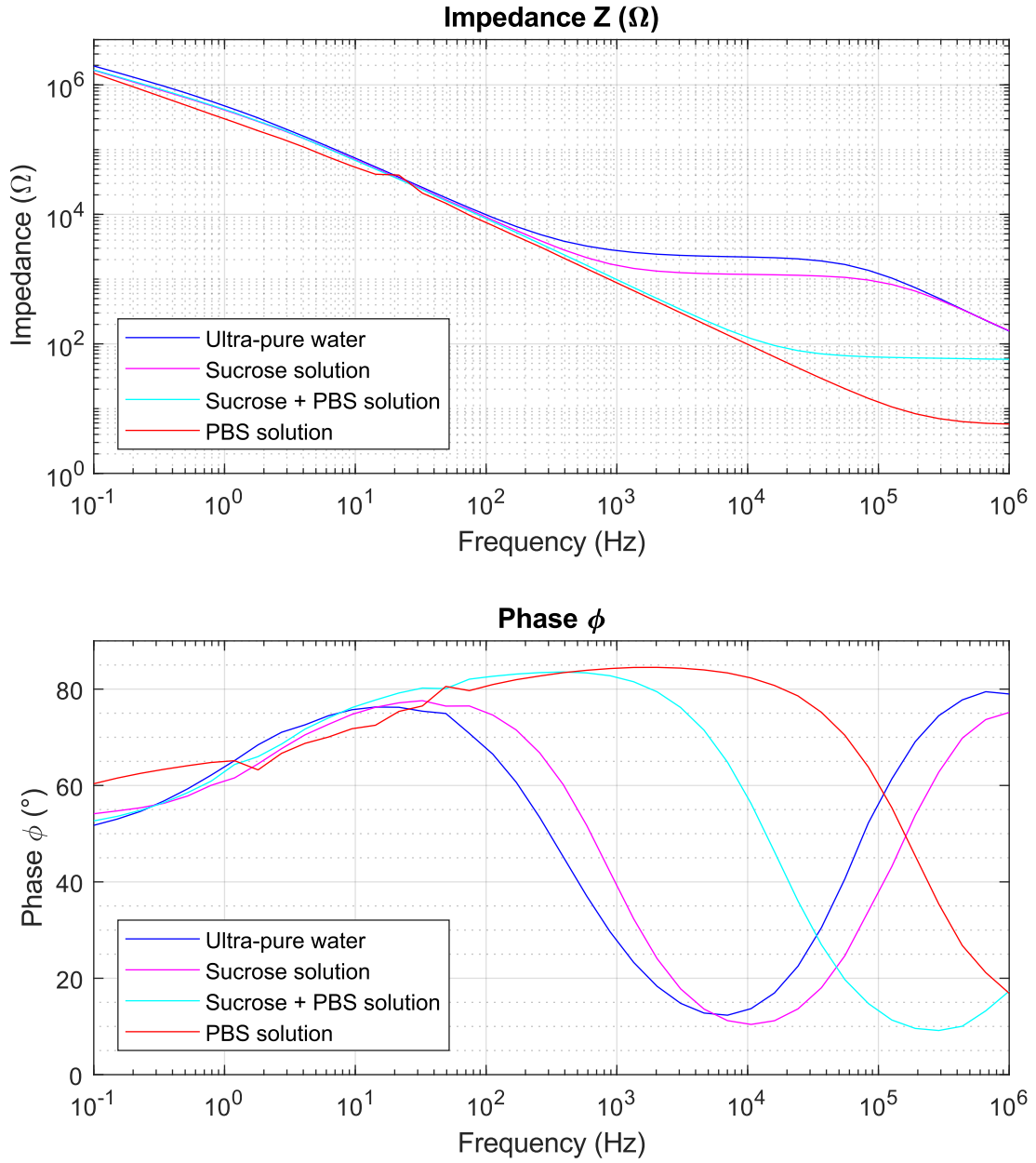


Figure 14: Impedance and phase diagrams (Bode Plots) for four different electrolytes. The respective conductivities can be found in table 3.

indicator, that the capacitive behaviour at high frequencies visible in the Bode plot may

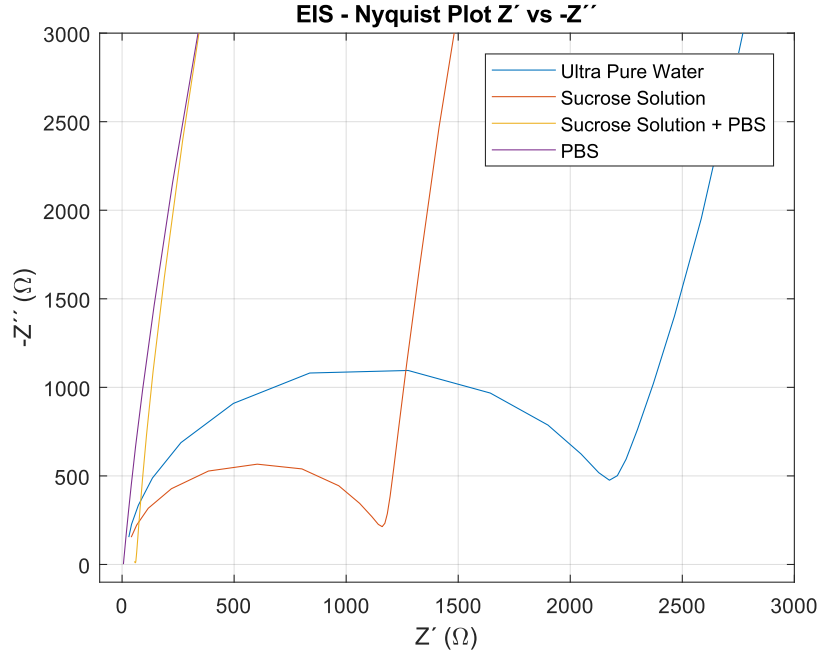


Figure 15: Nyquist plot for four different electrolytes. The respective conductivities can be found in table 3.

origin from geometrical characteristics of the passivized electrodes.

Secondly, as visible in the logarithmic depiction of the Nyquist diagram in figure 16, at very low frequencies all graphs converge to the same linear slope, independent from solution conductivity. This implies a state of the system, in which all configurations share a common dominating factor. An explanation could be a depletion of charge carriers in the bulk, due to a long period of time between subsequent changes in polarity (applied voltage). In other words, the ions have long accumulated at the electrode-electrolyte interface and create, firstly, a solution with high resistance (Z') in the inter-electrode space and, secondly, a highly charged (capacitive) region close to the electrodes (Z'').

Without contradiction, the linear slope shows that below a certain critical frequency, any additional impedance is composed in approximately equal ratio of a real *and* imaginary part. As described in section 2.2.1, this is the case for a constant phase element, or even Warburg diffusion impedance ($\alpha = 0.5$, or $\text{Im}(Z)/\text{Re}(Z) = 1$). Therefore one can conclude, that diffusion becomes the defining factor, creating a non-ideal capacitance, which accounts for both the increase of Z' and $-Z''$.

For the sake of completeness it shall be noted, that no significant difference between flowing and resting PBS solution in their respective Bode and Nyquist diagrams was observed.

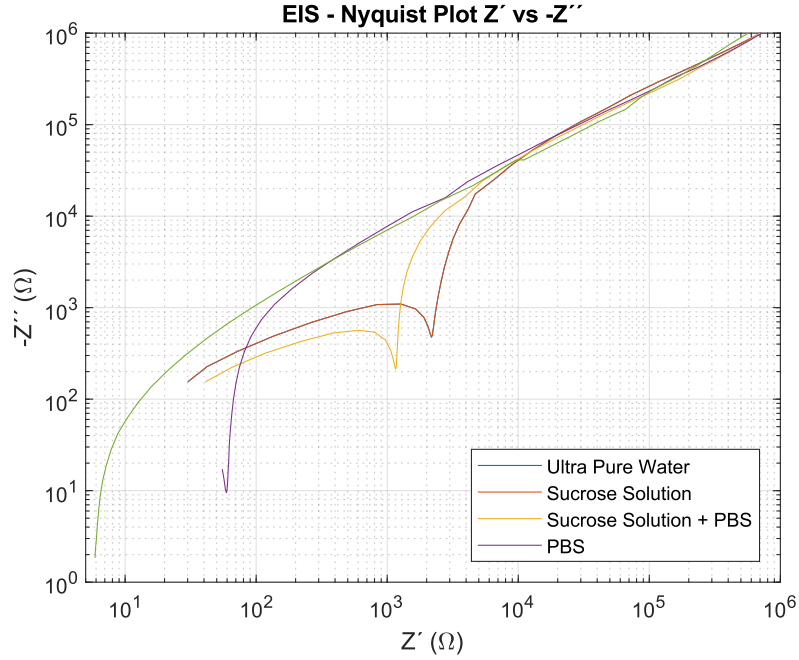


Figure 16: Double-logarithmic depiction of the Nyquist diagram in figure 15. At very low frequencies all graphs converge towards the same linear slope, which is characteristic for a constant phase element / Warburg impedance and is connected to double layer and diffusion phenomena.

4.3 Electrical determination of System elements

4.3.1 Diode Characteristic

The passivation layer consists of thermally oxidized titanium. Not only does it show extremely high permittivity or electrical resistivity, but as an n-type semiconductor it is also an electro-active material. Theoretically, together with the titanium substrate, it forms a Schottky diode.

The possibility of having two contrarily oriented diodes, as would be the case in the design of the ECMD device, creates a strong need for further investigations. Therefore, diode characteristics were extracted from two different sets of oxidized titanium sheets, using the technique described in section 3.2.2 and 3.2.3. The two sets are called *Standard* & *Polished Samples*. The standard procedure yields a compact 600-800 nm passivation layer by thermal oxidation. The polished sample differs from the standard version in that its surface has been mechanically polished.

Standard Sample Discussion

In figure 17 we see a depiction of the measured diode characteristic for four different samples produced as standard electrodes (S). At first glance, we can confirm that the examined specimen indeed behaves like a diode - we see the very typical V/I curve with forward current, threshold voltage V_{Th} and leakage current. A clear breakdown voltage is not visible.

The threshold voltage lies consistently within 3.5-4.5 V. This is exceptionally high compared to silicon diodes, with a V_{Th} of approximately 0.7 V. Also, the typical V_{Th} for Schottky diodes lies within 150-450 mV, which is an order of magnitude lower than observed in our case. This leaves room for further studies.

What is more, clear deviances between different standard specimen are visible. This concerns both their respective differential resistance at higher voltages than V_{Th} (the slope of the V/I curve) as well as leakage currents below -4 V.

When examining the negative voltage range, the course of the leakage current is not always a steady curve. While S_1 and S_2 show a plausible steady course with good current blocking, S_3 and S_4 are corrupted with chaotic and unstable artifacts, implying inferior oxide layer quality or deficient sample preparation.

Once again it has to be emphasized, that both our measurement setup and the manufacturing process substantially rely on manual intermediate steps. Therefore, a certain dispersion in element characteristics is unavoidable.

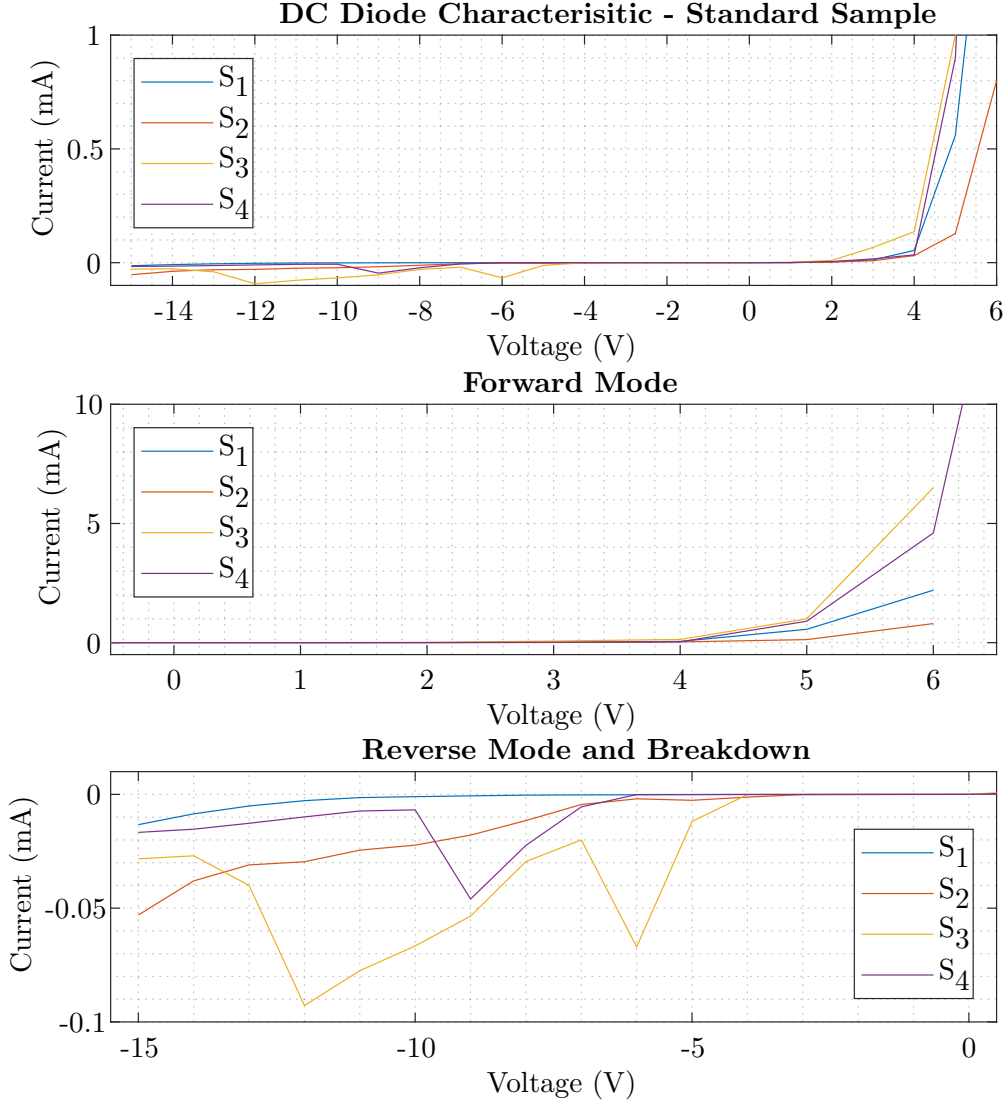


Figure 17: Diode characteristic for a Schottky Diode consisting of a Ti-TiOx-Ag junction. TiOx was synthesized using the standard procedure. All plots depict the V/I curves for four different specimen at a voltage range of -15 to 6 V. Plot (1) gives an overview over the diode characteristic. Plot (2) depicts the threshold voltage V_{Th} and forward current, revealing a high V_{Th} of approximately 4.5 V. Forward currents strongly depend on the individual sample. Plot (3) shows the negative working region, revealing either good leakage current suppression and a steady curve ($S_{1,2}$), or a very unstable curve ($S_{3,4}$). $I_{Leakage}$ remains low for all samples, with values well within the sub 100 μA range.

Polished Sample Discussion

The polished titanium oxide samples (P) were subjected to the same experimental setup. In this case, however, only two specimen were investigated with two respective experiment runs. P_{xy} refers to sample x and experiment number y .

Similar to the standard sample results, we see a well defined diode characteristic. The threshold voltage V_{Th} for P_1 is located at approximately 2.5 V, while for P_2 it can be found at a much higher voltage, at about 3.5 to 4 V.

Leakage current suppression can be found until -5 V, after which we see a gradual and smooth increase in leakage current, that runs out at $I_{Leakage} = [-0.1...-0.15]$ mA for P_1 and $I_{Leakage} = [-0.53...-0.72]$ mA for P_2 at a working point of -14 V, respectively. Therefore, $I_{Leakage}$ is one order of magnitude higher than with the standard passivation (S).

In comparison to the S samples, P exhibits a much higher degree of stability in terms of V/I curve smoothness. Contrary to S , unsteady artifacts in the reverse mode region are practically absent. What is more, the second measurement run reveals reproducibility of results, since both graphs, that belong to each respective sample, run in close proximity to each other. However, the consistent leakage current increase of approximately 50% in the second runs demands specific attention. If this is due to some sort of hysteresis, heating effects or a hidden destructive component in the measurement setup, is not clarified within this work. However, this data feature is worth to be studied further.

Conclusively, it can be stated with a high degree of certainty, that a side effect of using this kind of passivated electrodes for the ECMD is the introduction of two contrarily oriented diodes.

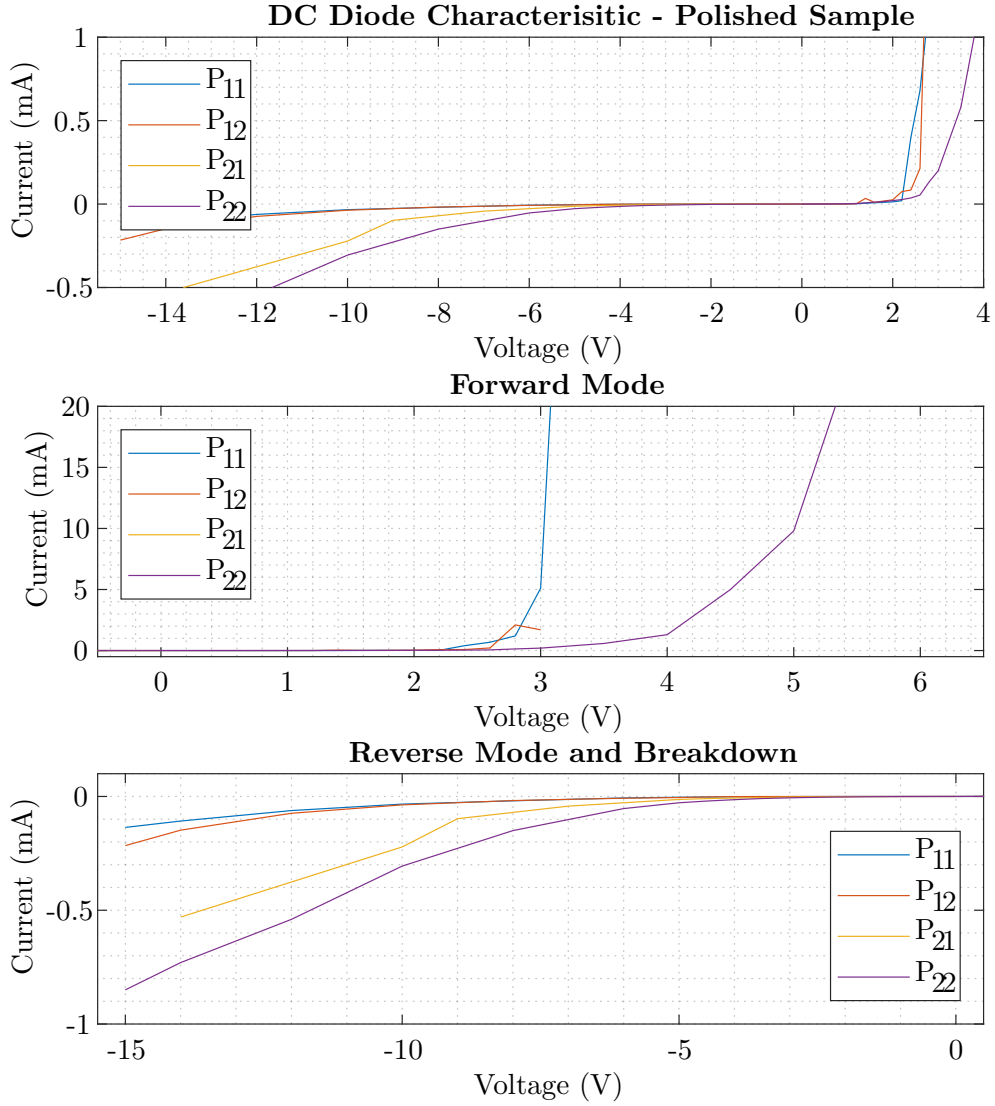


Figure 18: Diode characteristic for a Schottky Diode consisting of a Ti-TiOx-Ag junction. The TiOx standard sample underwent an additional polishing step. All plots depict the V/I curves for two different specimen, measured twice, at a voltage range of -15 to 6 V. The first plot gives an overview over the diode characteristic. The second plot reveals a high V_{Th} of approximately 2.5 & 4 V, that heavily depends on the individual sample. Thirdly, the last plot reveals a stable leakage current suppression, however, with $I_{Leakage}$ one order of magnitude higher than for standard samples.

4.3.2 Electrode Bath Experiments

Numerous different parameters need to be twitched and tuned in order to attain good lysis or transfection rates. Basic parameters include (but are not limited to) electrolyte conductivity, applied voltage amplitude, pulse duration and form as well as frequency. They define the target variable, which, in its most general form, can be specified as the spatial and transient potential profile within the electrolyte.

The potential curve is of special interest, since it allows conclusions about the internal electric field strength, which is believed to be the driving force behind electroporation phenomena. The measurement of two potentials over a distance (Δx) allows for the calculation of a potential difference ($\Delta\varphi$), which is proportional to the local current density/field strength.

However, the superposition of the diode characteristics of the opposed passivized electrodes poses a remarkable element of obfuscation. Moreover, the formation of a diode characteristic is dependent on the voltage drop over the respective pn-junction or, in case of a Schottky diode, over the semiconductor-metal interface. This voltage drop, in turn, depends also on the frequency dependent formation of the double layer at the passivation-electrolyte interface. To the best of our knowledge, the resulting behaviour can not be directly measured. Therefore, a way of visualization was sought, that captures the sum of those effects for a qualitative evaluation, which eventually led to the introduction and application of the bath setup.

The bath setup, as described in section 3.2.5, is a simple yet transparent tool for insight generation. On its basis, extensive experiments were conducted to determine each parameter's role and effects on the transient potential profile within the electrolyte.

Influence of Different Ions (LiCl, MgCl₂, KCl) on the Loading Curves

In order to determine, if different ions lead to different potential distributions within the electrolyte, solutions based on miscellaneous salts, yet with similar conductivities, were produced. In more detail, buffer solutions with Magnesium Chloride (MgCl₂), Lithium Chloride (LiCl) and Potassium Chloride (KCl) were mixed, while a conductivity interval of 155 to 166 $\mu\text{S}/\text{cm}$ was maintained.

In the process, information on the reliability of the *Bath Setup* can be gathered. For this purpose, not only were the measurement runs done with the standard titanium oxide electrodes, but also with gold sputtered glass. The results of these confirmation ventures can be found in the following.

Loading Curves with Gold Plated Electrodes

Results for KCl are depicted in figure 19. A rectangular pulse V_0 with a voltage amplitude

Salt Type	Peak Voltage	Frequency	Pulse Form	Conductivity
KCl	± 20 V	1 kHz	Square	156 ($\mu\text{S}/\text{cm}$)
MgCl ₂	± 20 V	1 kHz	Square	155 ($\mu\text{S}/\text{cm}$)
LiCl	± 20 V	1 kHz	Square	166 ($\mu\text{S}/\text{cm}$)

Table 4: Experiment specification. *Bath Setup* experiment with gold plated electrodes, different ion types and similar conductivities.

of ± 20 V was applied. The electric potentials $V_{1,2}$ at the sensing probes within the electrolyte record a potential curve representing a negative exponential decay. For V_2 this curve can be approximated as

$$V_2(t) = 20 (1 - e^{-(t+2\mu\text{s})/\tau}) - 10 \quad (4.2)$$

with $t \in [-2...20] \mu\text{s}$ and $\tau = RC$. R is associated with the bulk resistance, following equation 4.1 with A as the cross section of the active electrode area. C is assigned to the polarization of the electrolyte.

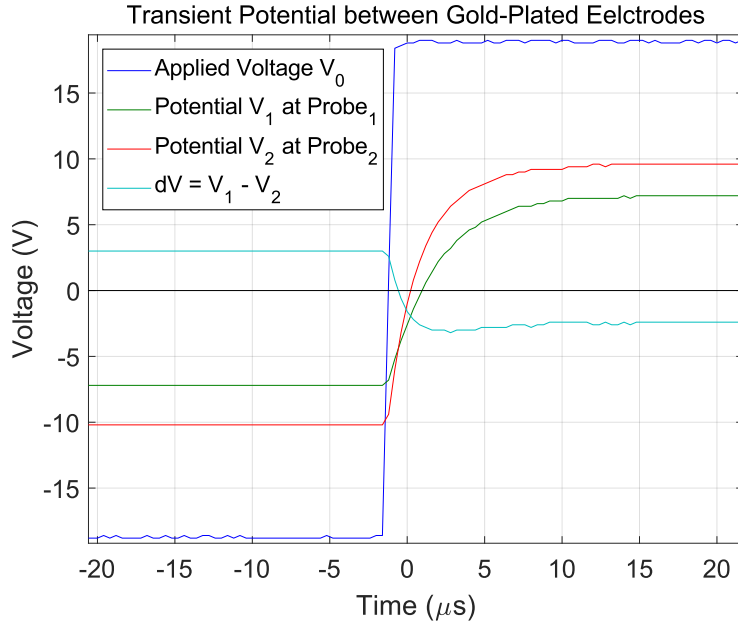


Figure 19: Loading curve using KCl as an example, extracted by the bath setup. Depicted are the applied voltage V_0 , potentials $V_{1,2}$ sunk into the electrolyte at the respective locations $x_{1,2}$, as well as the potential difference $dV = V_1 - V_2$. The measured potentials follow a negative exponential decay as the charge carriers move towards the electrodes and repolarize the electrolyte. $\Delta\varphi$ shows a gradual adjustment with a small overshoot of around 25% that lasts approximately 10 μs .

In figure 19 four plots are depicted - the applied voltage V_0 , the potential curves $V_{1,2}$

at the two sensing probes immersed into the electrolyte and the potential difference $dV = \Delta\varphi = V_1 - V_2$.

V_1 and V_2 follow a distinctive exponential timeline, as expected of a parallel RC-element, as the polarity of the applied voltage switches and the charge carriers move towards the electrodes. The geometrical centering of the probes in the setup invokes a similar pattern in the potential graphs. This is due to the voltage divider between the resistance between the probes and their respective resistances to the electrodes. The terminal potentials level at approximately ± 7 and ± 10 V.

After repolarization effects subsided, $\Delta\varphi$ forms a DC signal. As the applied voltage inverts, this potential difference, which is proportional to the internal electric field strength, does not switch polarity instantly, but builds up with a finite velocity and a small overshoot of around 25 % that last approximately 10 μ s. Afterwards, a symmetric terminal potential difference sets in.

The experiments with MgCl_2 and LiCl show similar results and plots are therefore left out.

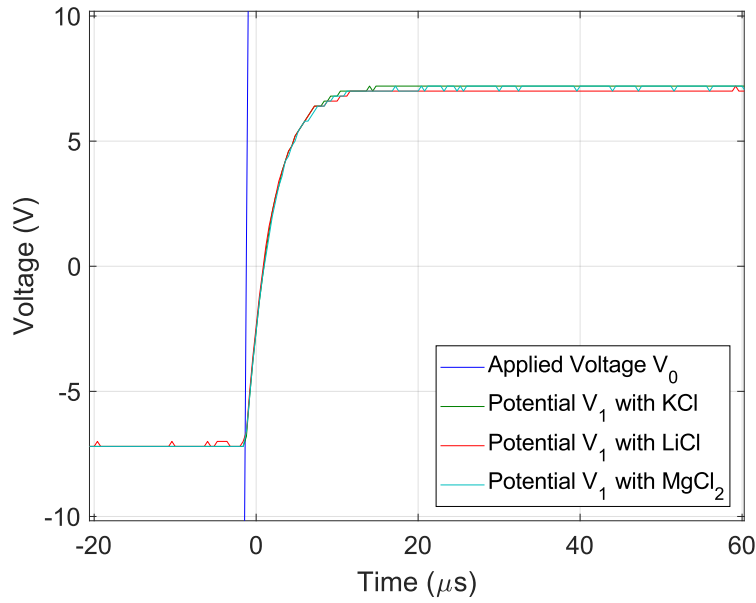


Figure 20: Potassium chloride, magnesium chloride and lithium chloride solutions with equal conductivity (155-166 $\mu\text{S}/\text{cm}$) show the exact same loading kinematics and terminal potential drop under equal experimental conditions, in accordance with Ohm's Law.

Figure 20 shows the loading curves for all used ions at the sensing Probe 1. Potassium chloride, magnesium chloride and lithium chloride solutions with equal conductivity show the exact same terminal potential drop under equal experimental conditions, in

accordance to Ohm's Law. Since bulk conductivity depends on the ion mobility, we also see the expected equal loading kinematic, adding credibility to the Bath Setup as an experimental setup.

Loading Curves with Passivated Electrodes using Titanium Oxide

In figure 21 we see a depiction of the transient potential when passivated electrodes are used. Figure 21.a) shows the potential transition at the moment of changing polarity in more detail. At first glance, the loading curves look very similar to the ones obtained under simplified conditions - that is, with a gold-electrolyte interface, instead of a TiOx-electrolyte junction. V_1 and V_2 show a capacitive curve, resembling a negative exponential decay.

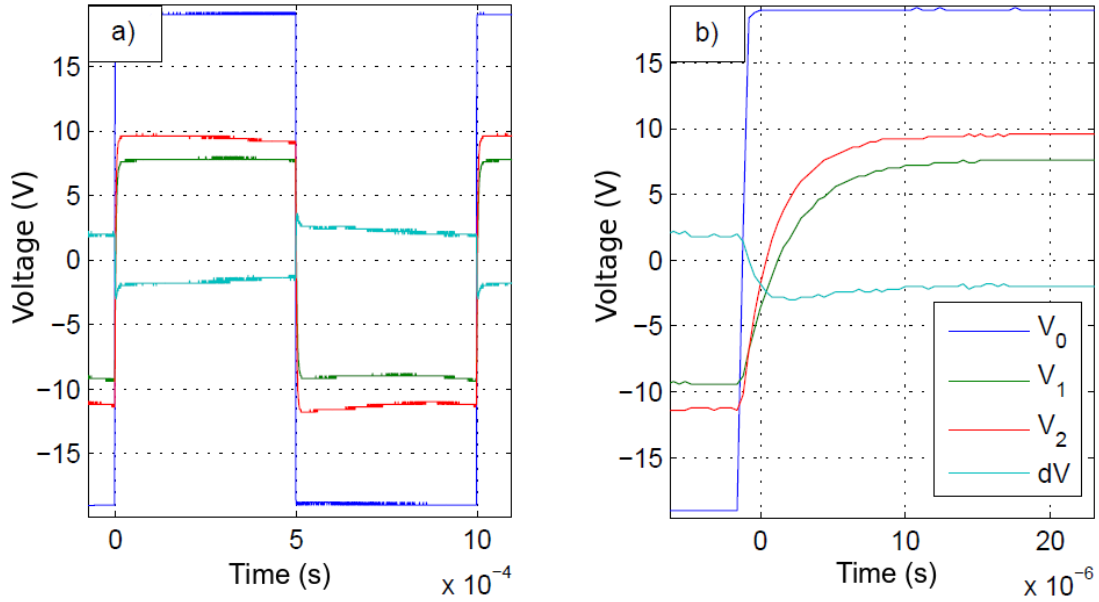


Figure 21: Loading curves for KCl with a conductivity of $156 \mu\text{S}/\text{cm}$ in a Bath Setup using passivated (oxidized titanium) electrodes. Applied Voltage V_0 , probe potentials $V_{1,2}$, potential drop $dV = V_1 - V_2$. a) shows the whole pulse and a non-linear, polarity-independent decline in V_1 & V_2 . Also, a distinctive asymmetry in terminal dV is visible. b) shows the area of polarity change in more detail. Visible are exponential loading curves similar to a Bath Setup with gold electrodes, however, the overshoot in dV is more pronounced with 50%.

However, there are two major differences visible in 21b). Firstly, the overshoot of the potential drop dV is significantly larger, with +50% compared to the adjacent post-peak voltage (-3 V vs -2 V & 3.6 V vs 2.4 V), in contrast to 25% using the gold-electrolyte interface.

Secondly, there is a pronounced asymmetry in terminal potential visible in figure 21a), just before the reversal of polarity. For V_2 we have terminal values of 9.2 V and -11.2 V and for V_1 7.8 and -9.2 V, resulting in a relative potential shift to the negative range of 22% and 18%, respectively. This asymmetry is due to a non-linear skew, 'pulling' the potential curve to the negative, independent from polarity. However, the full formation of this phenomenon, which is only slightly indicated here, will be visible later at higher bulk conductivities.

Figure 22 sheds further light onto the details of the potential drops dV in KCl, LiCl and $MgCl_2$ electrolytes as well as in ultra-pure water (mQ). The aforementioned overshoot is now put into perspective and can be described as a distinctive peak. Interestingly, the magnitude of the respective peaks is the same for all used electrolytes, provided they share the same conductivity. This is also the case for dV KCl_{gold} , which marks the potential drop using a gold sputtered electrode instead of titanium-oxide.

Moreover, unlike dV KCl_{gold} , which quickly reaches a rather stable terminal voltage after peak abatement, all other potential drops pass over to a rather stable linear decay in direction of the grounding potential - the instability is due to quantization noise, which is hard to filter. This decay is approximately $\pm(1.37 + 1.17)/2 = \pm 1.27$ V/ms.

An interesting exception from the above mentioned observations poses ultra-pure water. Neither does it show such a distinct peak (only 12% overshoot), nor does it exhibit any significant asymmetry.

Furthermore, figure 22 elucidates the peak dynamics. It is apparent, in more detail, that indeed all electrolytes with a conductivity of $160 \mu S/cm$ reach the peak voltages of around 3.65 V and -3 V, respectively. Peak durations are 10-15 μs .

Furthermore, we see a small, yet definite, jump of approximately 0.5 V for dV mQ at the polarity transitions, that is absent in all other electrolytes.

Rectification Effects by Titanium Oxide

In this chapter, effects imposed on the potential profile by the Schottky Diode will be elucidated. For this purpose, the highly conducting PBS solution ($1.6 mS/cm$) was used, due to the consequential low electrolyte resistance. As a result, the coating becomes the most dominant element in the system and its effects can be studied more easily.

Figure 23 illustrates how the oppositely oriented electrodes with their respective diode characteristics shift the whole potential profile away from a symmetric distribution and towards the negative range. This does not mean, however, that the internal field strength / current shows an asymmetry. Clearly, the potential difference dV remains within the quantization noise, so no conclusive claims can be made in this regard.

An explanation for this potential distribution is provided in figure 24. In our setup, one

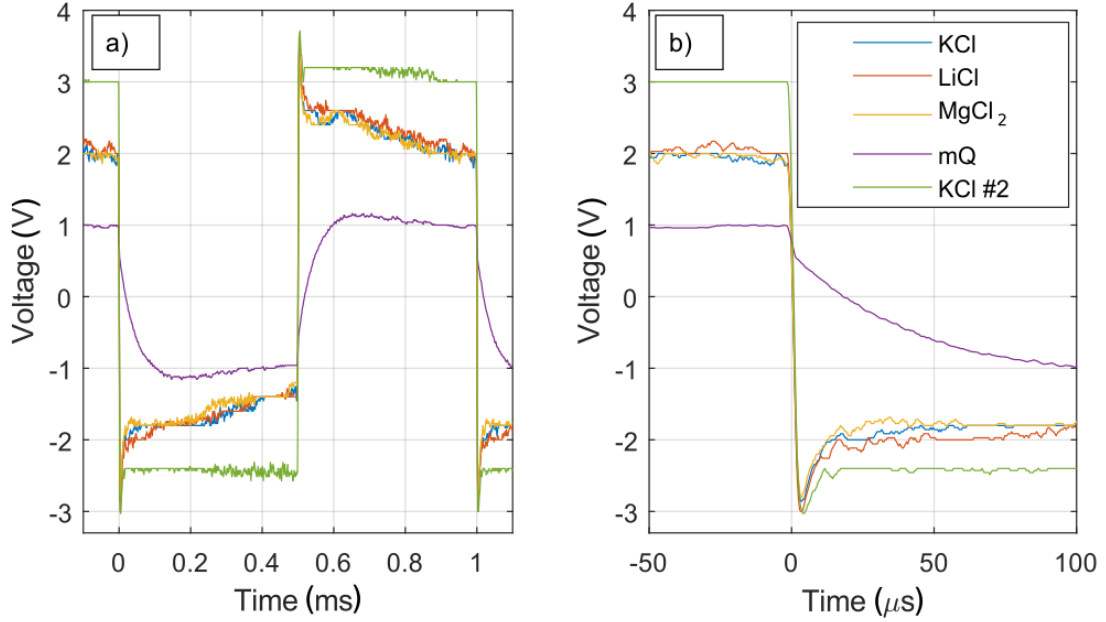


Figure 22: Transient potential drops between two sensing probes in different electrolytes with a conductivity of $160 \mu\text{S}/\text{cm}$ and ultra-pure water (mQ) in a Bath Setup using passivized (oxidized titanium) electrodes. KCl_{gold} refers to a comparative loading curve from a KCl electrolyte in a Bath Setup with gold electrodes. In a) a distinctive peak at the time of polarity change is visible, where all electrolytes with similar conductivities reach the same peak voltage. All suspensions in titaniumoxide show a subsequent linear decline of approximately $1.27 \text{ V}/\text{ms}$. An asymmetry of 20% is evident. Ultra pure water shows no asymmetry and a significantly smaller overshoot of only 12%. In b) peaks are depicted in more detail. All electrolytes reach common peak values of approx. 3.65 V & -3 V . Peak durations are between $10\text{-}15 \mu\text{s}$. mQ shows a distinctive jump at time of polarity change. Note the different time scale compared to a).

electrode is always grounded at the 0-potential, while the other alternates between, for example, 20 V and -20 V . Depending on the polarity, either electrode causes a substantial potential drop, as it will function as a blocking diode, while the other has a rather small impedance, as it will work in the forward mode. As a result, the intrafluidal potential will always converge to a region close to the respective lower potential.

However, a closer look at figure 25, which depicts the potential profile for ultra-pure water at a frequency of 10Hz , reveals a new feature. Between the polarity change and the conversion to the terminal rectified potential distribution, a distinct voltage shift is visible. This peak's most interesting characteristic is its polarity independence of the applied voltage.

Indifferent of V_0 's sign, it poses a temporary displacement to the positive direction.

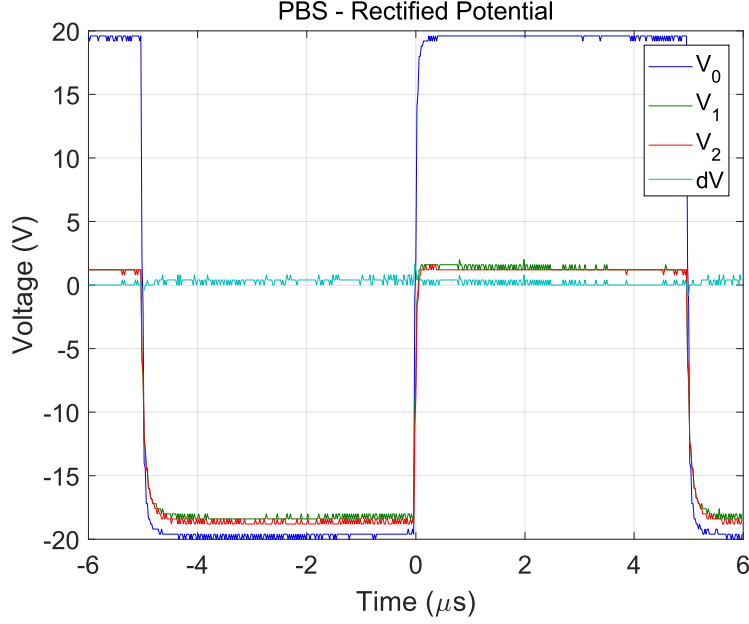


Figure 23: Potential curves at a frequency of 100 Hz in PBS with a conductivity of approximately $1.6 \times 10^3 \mu\text{S}/\text{cm}$ and the applied voltage V_0 , the sensing potentials $V_{1,2}$ and the potential drop between the sensing electrodes dV . There is a strong rectification effect due to the voltage dependent passivation. dV remains in the order of the quantization noise.

Furthermore, it is superimposed on the voltage jump of $V_{1,2}$'s terminal values (This jump is in the order of V_0 and occurs when the applied voltage changes its sign).

The clear uni-directional behaviour suggests a process related to the passivation, which functions as a Schottky Diode. However, the underlying physical process remains obscure. A brief analytic examination follows in figures 26 and 27.

It shall be noted beforehand, that in contrast to the PBS sample, we see a clear potential difference dV in the second half-period with ultra-pure water. An explanation could be the asymmetry and parameter variance of the two opposed passivation layers. In figure 25 we see, that $V_{1,2 \text{ terminal}}$ is significantly closer to the 0-potential in the second half period, than it is in the first to the potential V_0 .

A possible scenario is, that passivation D_2 , in reference to figure 24, has a "more ideal" forward characteristic, leading to a negligible voltage drop at D_2 and thus a $V_{1,2 \text{ terminal}}$ closer to the 0-potential. Furthermore, this can explain the more pronounced bulk voltage drop dV , since the whole system is still a voltage divider. The peak of dV in the second half-period fits surprisingly well to the gap between terminal $V_{1,2}$ and V_0 in the first half-period. This thought experiment is visualized in figure 24 as a purple, dashed potential curve.

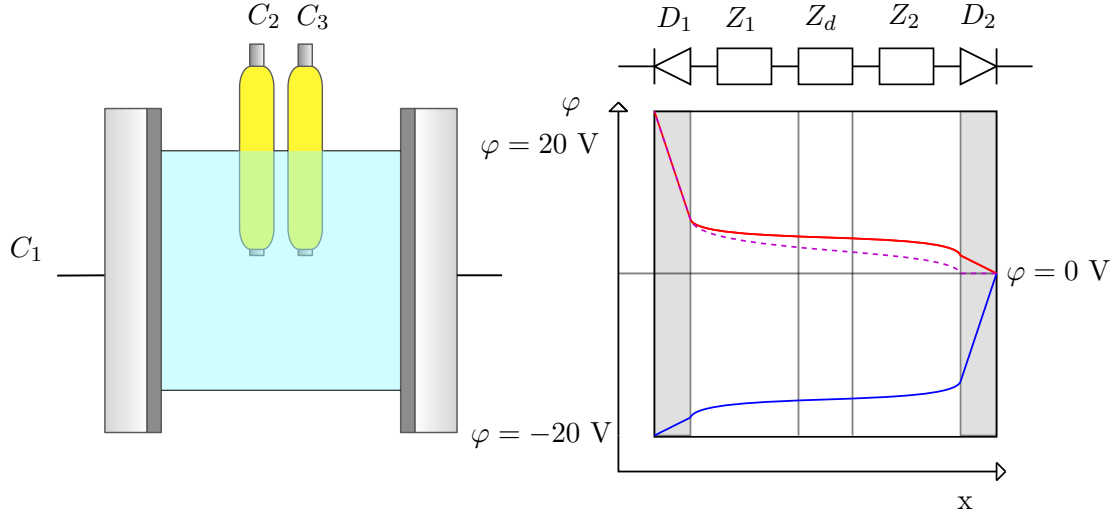


Figure 24: Intrafluidal Potential in presence of diodic electrodes after all transient processes are completed - with passivized electrodes $D_{1,2}$, double layer and bulk impedances $Z_{1,2}$ and the impedance Z_d between sensing probes.

Asymmetric Peak Analysis

In the following, the asymmetric post-polarity-switch peak from figure 25 shall be examined in more detail.

Several experimental runs were conducted, including with varying applied frequencies. Specifically, potential curves for ultra-pure water were recorded for a frequency range of 1 Hz to 100 kHz. It was observed, that the above mentioned peaks only occurred between 1 Hz and 500 Hz. What is more, the pulse duration shows a significant non-linear dependence on the frequency.

In order to quantify this relation, in figure 26 the respective half-periods are plotted in a way that allows a detailed comparison. Since we have signals at different frequencies, the respective half-periods are visually stretched. Tangents were laid onto the inflexion points of every pulse. All slopes converge to one point, indicating that the pulse can be approximated as

$$p(t) = A_1(1 - e^{-t/\tau_1}) A_2(e^{-t/\tau_2}), \quad (4.3)$$

a combination of two competing (re-)loading processes with $\tau_1 \ll \tau_2$.

As shown in figure 26, those tangents are then intersected with the value of the terminal voltage, yielding a measure for a characteristic time constant τ , which for a parallel RC-element is $\tau = RC$. For ultra-pure water in the aforementioned experimental setup, those time constants can be found as follows:

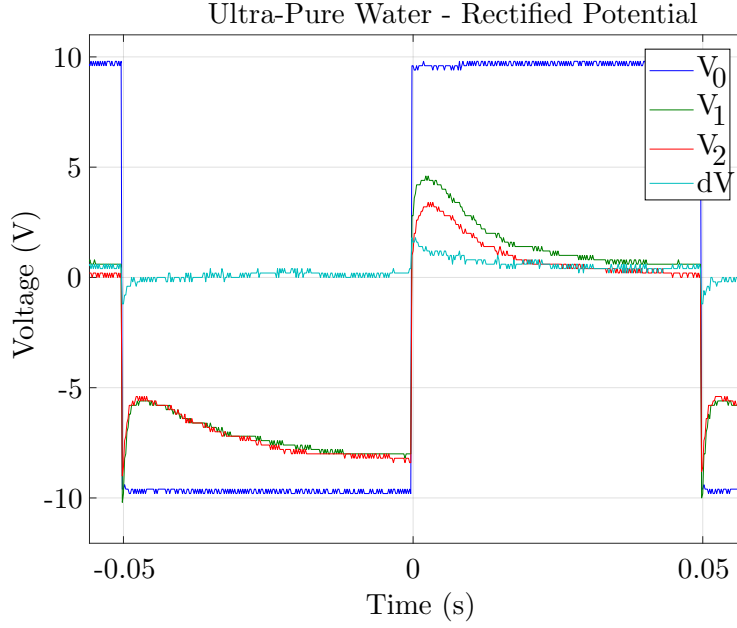


Figure 25: Potential curves at a frequency of 10 Hz in ultra-pure water (mQ) with a conductivity of $3 \mu\text{S}/\text{cm}$ and the applied voltage V_0 , the sensing potentials $V_{1,2}$ and the potential drop between the sensing electrodes dV . At the time of polarity change, the potential jumps with V_0 and subsequently shows a distinctive asymmetric pulse to the positive direction. Afterwards, the internal potentials converges to a strongly rectified signal as a result of the voltage dependent passivation. In contrast to PBS, dV shows a significant magnitude in one half-period.

Frequency	Time constant τ
1 Hz	55.2 ms
10 Hz	16.3 ms
50 Hz	7.8 ms
100 Hz	7.1 ms
500 Hz	3.8 ms

Table 5: Characteristic time constants for ultra-pure water at different frequencies.

In the next step, a brief data exploration suggests a linear relationship, when mapped onto the double-logarithmic space. Figure 27 illustrates all pulse widths τ over frequency on a double-logarithmic plot.

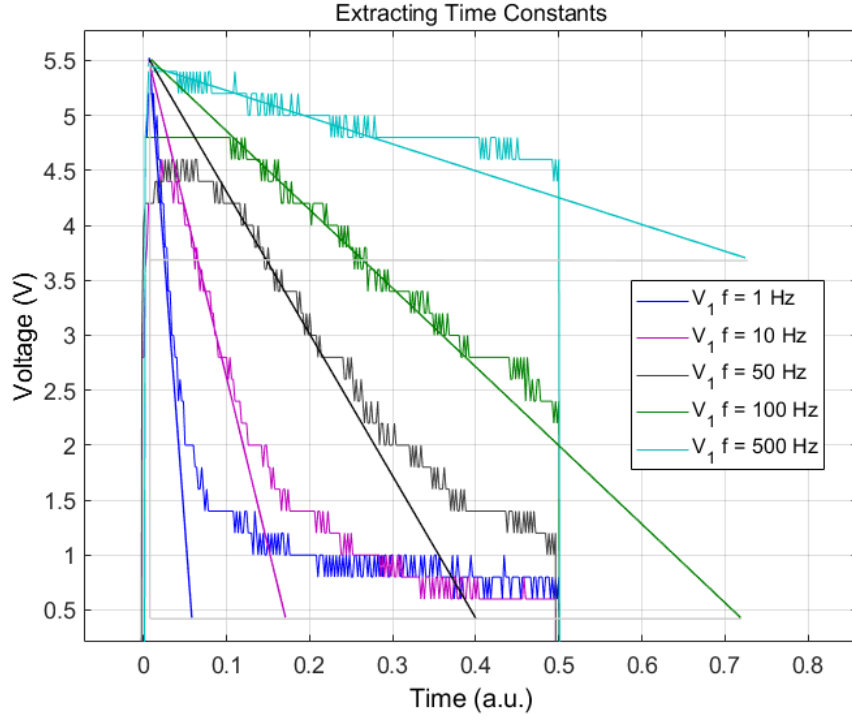


Figure 26: Comparison of loading peaks induced at different frequencies in ultra-pure water in a Bath Setup with passivated electrodes. Furthermore, illustration of the graphical strategy for extraction of approximate time constants τ .

A linear regression can be performed in the logarithmic space, yielding the relation

$$y = k x + d$$

$$\log(\tau) = -0.45 \log(f) - 1.3. \quad (4.4)$$

This can be translated to

$$\begin{aligned} \tau(f) &= f^{-0.45} e^{-1.3} \\ &= \frac{1}{\left(\frac{\omega}{2\pi}\right)^{0.45}} e^{-1.3} \\ &\approx \frac{1}{\sqrt{\omega}} \text{ const.} \end{aligned} \quad (4.5)$$

We can now attain an approximation for the dominating capacity. We substitute τ in $\tau = R C$ and reach

$$C = \frac{1}{\omega^{0.45}} 1/R \text{ const.} \quad (4.6)$$

Theoretically, R can be calculated by geometrical considerations and the electrolyte conductivity in the form of equation 4.1. Using the ideal capacitor as an approach for the impedance,

$$Z_{\text{Capacitor}} = \frac{1}{j\omega C}, \quad (4.7)$$

we arrive at

$$\begin{aligned} Z &= \frac{1}{j\omega^{\frac{1}{\omega^{0.45}}}} \frac{R}{\text{const.}} \\ &= \frac{1}{j\omega^{0.55}} \frac{R}{\text{const.}} \\ &\approx \frac{1}{j\sqrt{\omega}} \text{const.} \end{aligned} \quad (4.8)$$

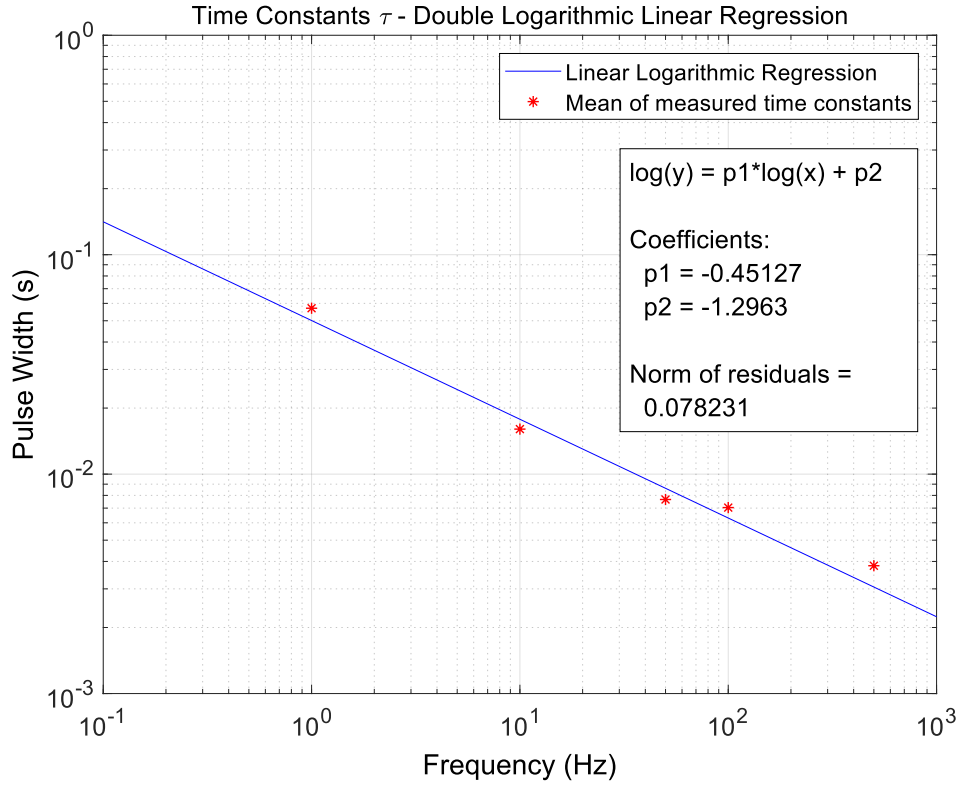


Figure 27: Double-logarithmic plot for characteristic times τ over the frequency f and linear logarithmic regression.

The extracted relation

$$Z \sim \frac{1}{j\omega^{0.55}} \text{const.} \quad (4.9)$$

shows a strong resemblance to the definition of the impedance for a Constant Phase Element $Z_{\text{CPE}} = \frac{1}{(j\omega)^n Q}$ or even Warburg Element $Z_{\text{Warburg}} = \frac{1}{\sqrt{j\omega} Q}$ (equations 2.6 and 2.7). Those elements are used to model distributed capacities, for example diffusion processes, double layers and imperfect dielectrics (see section 2.2.1).

An educated guess for the origin of the peaks in question is therefore an interaction process between dissolved ions, acting as charge carriers (diffusion & double layers), and the passivation (Schottky Diode). What is more, the Schottky diodes need to establish a working point, which dynamically depends on and interacts with the ion distribution in proximity of the passivation-electrolyte interface. Due to the very high time constants in the low frequency range, it seems intuitive that diffusion plays the dominating role. Eventually, the system reaches a dynamic equilibrium.

4.4 Equivalent Circuit

4.4.1 First Approach

As described in section 3.2.4, several Electrical Impedance Spectroscopies (EIS) for electrolytes of various conductivity were recorded. EIS data delivers crucial data about an electric system. The provision of the real and imaginary part of an impedance and the corresponding phase shift over an immense frequency range allows for an all-encompassing modeling of the system in the form of an equivalent circuit, that is derived by fitting the impedance and phase shift curves. That way, one attains differential equations, that are solvable both analytically and numerically.

The included circuit elements ideally represent single isolated processes, but more often than not integrate a number of phenomena, that cannot be examined from EIS data alone. Usually, the mapping of different physical or chemical processes to impedances is of surjective nature.

The model's state variables are voltage and current amplitudes over each element at every point in time. After equivalent circuit derivation, such a model can therefore serve two goals:

Firstly, one parameter (e.g. a certain resistance of interest) can be identified and examined independently. For example, in our case our main goal is to assess the internal field strength, which is proportional to the voltage drop over the theoretically known bulk resistance. If we can isolate this resistance, we can conduct simulations even with a lack of understanding of the physical processes that the other circuit elements represent.

Secondly and substantially more challenging, the EIS data can be used to generate a representative model of all relevant processes at play. For this endeavour, information independent from the "black box" EIS data has to be used and, like variable substitution in an equation, has to be integrated in a concerted way. However, the lack of appropriate measuring techniques is often the very reason for consulting EIS data in the first place.

The derivation of the equivalent circuit shall be illustrated by the example of ultra-pure water (milliQ) EIS data.

The EIS results were fed into the simulation and circuit fitting software NOVA[®] 1.11 and reasonable boundary conditions were determined. Those boundary conditions include the basic structure of the circuit and the parameter range of each circuit element. Special attention has to be given to the circuit elements' initial values, since the fitting algorithm iteratively searches for better fits by parameter variation. Unfortunate initial values lead to unrealistic fitting parameters due to local minima in the cost function hyper plane.

An orientation for boundary conditions and matching of circuit elements can be gained by considering known geometrical dimensions, conductivities and physical structures of the examined device. Table 6 illustrates the information available prior to the fitting procedure.

	milliQ	Sucrose	Sucrose + PBS	PBS	TiOx
C	[791 ... 967] pF	-	-	-	[10.05 ... 296] nF
R	[2.44 ... 2.98] k Ω	[1.22 ... 1.49] k Ω	[43.9 ... 53.6] Ω	[4.58 ... 5.6] Ω	-
ϵ_r	80	-	-	-	[10 ... 85]
γ	3 $\mu\text{S}/\text{cm}$	6 $\mu\text{S}/\text{cm}$	167 $\mu\text{S}/\text{cm}$	1.6 mS/cm	-
l	81 $\pm 5\%$ μm	81 $\pm 5\%$ μm	81 $\pm 5\%$ μm	81 $\pm 5\%$ μm	[267 ... 839] nm
A	1 $\pm 5\%$ cm^2	1 $\pm 5\%$ cm^2	1 $\pm 5\%$ cm^2	1 $\pm 5\%$ cm^2	1 $\pm 5\%$ cm^2

Table 6: Theoretical values of system elements. Sources: [29], [32].

At first, an effort was made to reproduce the impedance and phase pattern by use of RC-elements only, since they represent ideal capacities and were expected to be easier to assign to certain processes. A circuit structure embedding an RC element for each suspected relevant process was defined. We may consider the Helmholtz Double layer, a Diffuse Layer, the bulk electrolyte, which also was expected to have a geometrical capacity, wire resistances and an overall capacity of the sandwich design. The resulting circuit is depicted in figure 28.

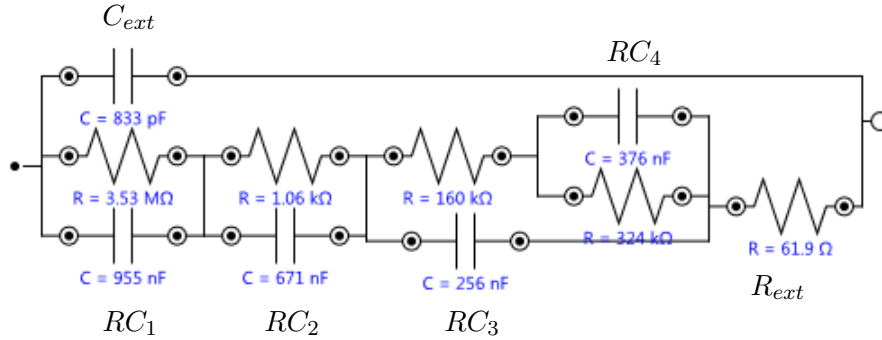


Figure 28: First approach for an equivalent circuit for ultra-pure water in the ECMD.

The Bode Plot in figure 29 gives an impression of the circuit's performance. The Impedance curve seems to be fitted rather well, while the phase shift graph shows alternating deviations in the lower frequency region of 0.1 to 100 Hz.

However, it must be critically noted, that with such a large number of RC-elements, the

user opens various degrees of freedom to the fitting software. As a result, an arbitrary impedance spectrum can be emulated, while the circuit itself provides little scientific value. Also in this case, any process or structure assignment is possible only to a limited extent. It shall be tried nonetheless in the following paragraph.

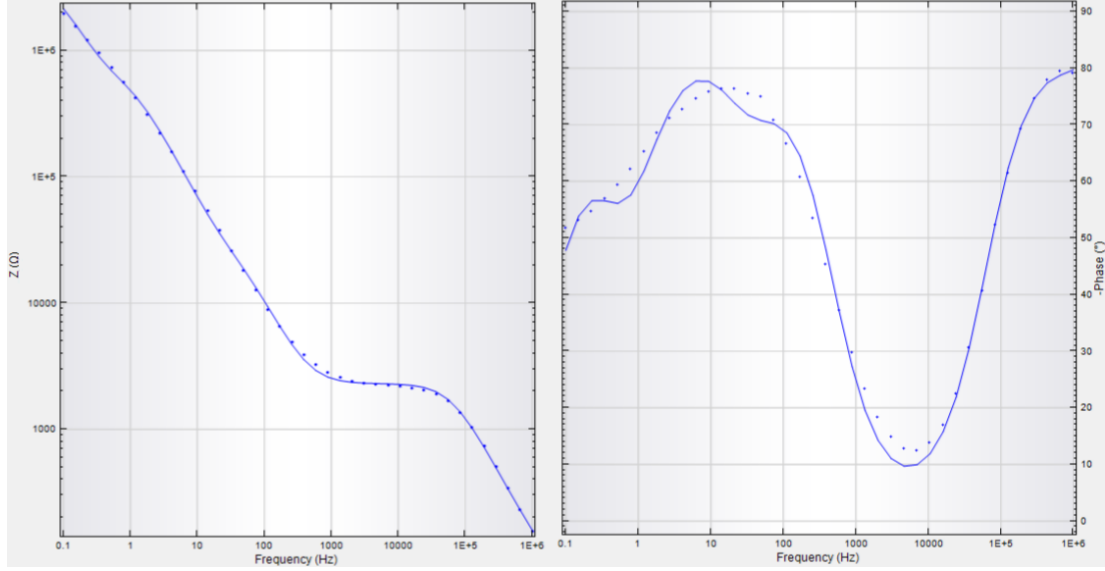


Figure 29: Bode Plot comparing the first equivalent circuit and EIS data (dotted line).

Firstly, there is a robust match between the theoretical capacity of the bulk liquid milliQ and C_{ext} . $C_{\text{ext}} = 833 \text{ pF}$ lies well within the projected range of 791 to 967 pF.

Furthermore, the interleaved RC element RC_3 shows a plausible capacity of 256 nF, which lies in the upper range of the theoretical oxide capacity of up to 296 nF. Consistently, we see a very high resistance of 160 kΩ, which can be interpreted as the blocking Schottky Diode.

The embedded RC element RC_4 can be construed as a correction element for modeling a frequency dependence of the oxide layer. This thought is supported by the characteristic time constant $\tau = RC$ of 0.12 seconds - relating to the low frequency of 8.4 Hz.

R_{ext} may be a superposition of polarization resistance of the electrolyte and supply resistance in the form of $R_{\text{ext}} = R_{\text{pol}} + R_{\text{supply}}$.

RC_2 is not fitted well to any theoretical parameter. However, this may be a mere mismatch due to an unfortunate starting value of R. So if we force a process upon this element other than impedance spectrum emulation, it has to be matched to the bulk electrolyte, since its resistor is at least in the same order of magnitude of the bulk resistance. Therefore, a possible fit correction would be to double R and halve C_2 , so that RC_2 's cut-off frequency $f_c = 1/\tau = (RC)^{-1}$ remains the same. This would lead to

a resistance of 2.12 k Ω , which is much closer to the projected bulk resistance.

Another element difficult to assign is RC_1 , which is unrelated to any theoretical value. With its extremely high resistance and capacity it is a candidate for the Helmholtz Double layer. However, it also shows a cut-off frequency of 0.3 Hz, which lies in the range of strong phase shift deviations from experimental values. Therefore, it cannot be ruled out, that RC_1 is merely a correction element, emulating an apparently more complex frequency dependent process dominating in the frequency range of 0.1 to 30Hz, as visible in figure 29.

Beyond the described assignment difficulties, the presented equivalent circuit shows other signs of inadequacy. For example, the matching solutions were relatively unstable, leading to significantly deviating final parameters, if boundary conditions are changed.

4.4.2 Coating Model

Ideally, a good model structure meets at least the following two conditions. Firstly, it bears a sensible degree of robustness towards changes in boundary conditions, such as the allowed parameter solution space or initial parameter values. Secondly, especially in our case, it is consistent and applicable to different application scenarios. Here, different bulk electrolytes are used, while the physical structure of the device stays the same. It is reasonable to expect major changes only at target variables closely related to the electrolyte.

The following simplified final equivalent circuit, depicted in figure 30, meets the aforementioned requirements of robustness and universal applicability. It is a combination of an RC element representing the bulk electrolyte as well as a nested circuit related to the so called *Coated Metal Model* (see section 2.2.2).

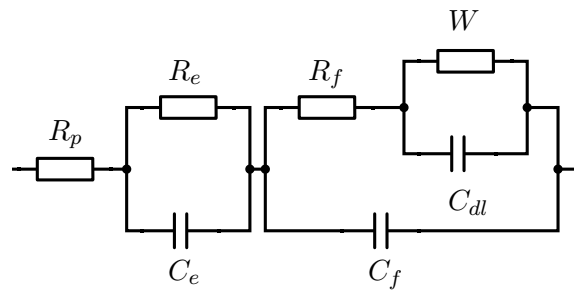


Figure 30: Final simplified equivalent circuit representing the ECMD for all electrolytes.

Figure 31 shows the improved performance of the equivalent circuit model. Artifacts

of the phase shift in the range of 0.1 to 50 Hz are eliminated by condensing several RC-elements into an interleaved RC-element including a Warburg impedance.

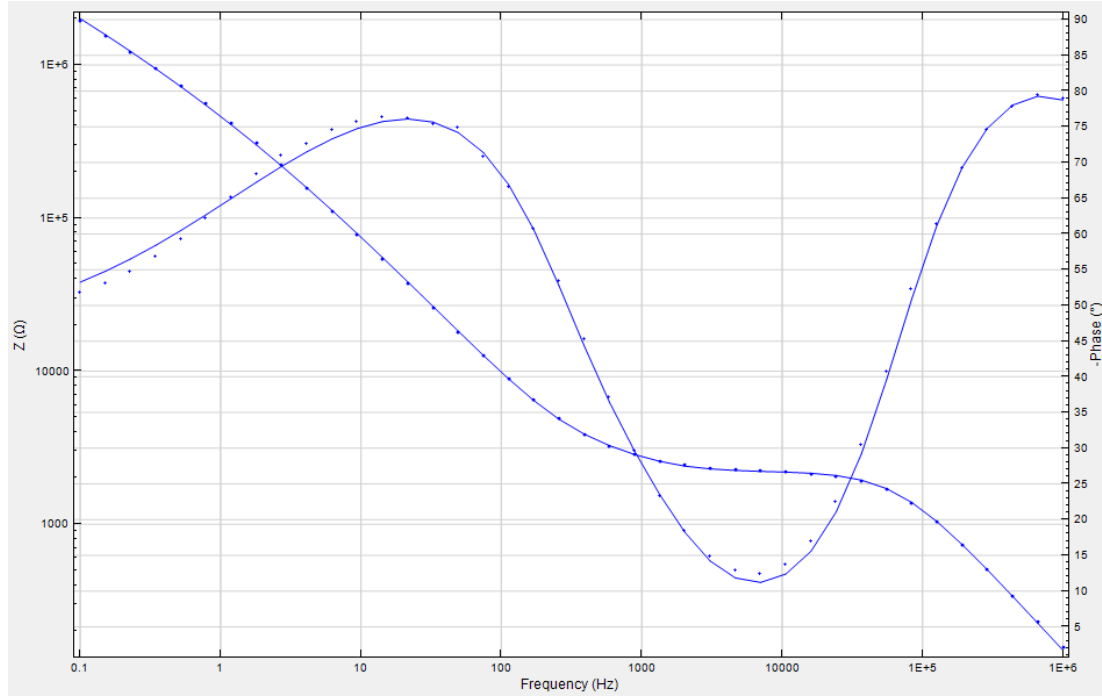


Figure 31: Bode Plot comparing the final model's impedance spectrum and EIS data (dotted line) for ultra-pure water. Especially in the low frequency range performance improved significantly.

As visible in figure 30, which depicts the final model design, the number of RC-elements was reduced while at the same time improving the impedance emulation performance. In the following section, the structure of the equivalent circuit, including a presumptive underlying physical representation for every circuit element, as well as the performance gains will be discussed in more detail.

4.4.3 Results

Table 7 illustrates all fitted values for every examined electrolyte. First, R_p will be examined in more detail. As the only resistor without adjacent capacitor, it takes a special position in the model. It functions as an offset resistance in the impedance spectrum with a rather stable magnitude of 19.4 to 24.7 Ω . A look at figure 14 reveals that it dominates the circuit behaviour only in a frequency region higher than 10^6 Hz. What is more, it diminishes for very high conductivities, as is the case for the PBS solution. Therefore, wire resistances can be excluded as cause. Instead, it seems like a polarization resistance, whose effect decreases with increasing ion concentration.

	Ultra-pure water	Sucrose	Sucrose + PBS	PBS
R_p	19.4 Ω	19.5 Ω	24.7 Ω	-
R_e	2.16 k Ω	1.14 k Ω	52.88 Ω	6.15 Ω
R_f	4.49 k Ω	3.53 k Ω	858.37 Ω	884 Ω
C_e	1.08 nF	1.06 nF	1.24 nF	4.18 nF
C_f	106 nF	136 nF	145.6 nF	150 nF
C_{dl}	56.9 nF	28.7 nF	18.4 nF	29.6 nF
W	530 nMho	653 nMho	662 nMho	786 nMho
$C_{dl} + C_f$	162.9 nF	164.7 nF	164 nF	179.6 nF

Table 7: Fitted values of the simplified equivalent circuit for four different electrolytes.

R_e represents the bulk solution resistance. It is in close agreement with theoretical values across all conductivities, as a comparison with table 3 and 6 shows.

Analogically, C_e can be assigned to the electrolytes' capacity, that is spanned up by its geometrical dimension and relative permittivity, similar to a plate capacitor. While C_e remains stable in the low conductivity range, a gradual increase from 1.08 nF to up to 4.18 nF is visible. An explanation may be given by the following thought: If approximated by a plate capacitor with $C = \epsilon_r A / l$, the physical dimension l may be reduced due to other processes, like diffusion, "taking up space", reducing l and thus increasing C . Then again, if an (unknown) process increased the relative permittivity ϵ_r , a higher C was the result as well. This requires further investigation.

This RC-element is of special interest for our modelling scenario, since the electric field strength within the electrolyte/cell suspension is directly proportional to the voltage drop over R_e .

The heart of the model is represented by the nested RC-element harbouring the Warburg element. Our findings are in conformity with Mitton et al.[24], who described roles of the respective circuit elements in this construct within a setting of polymer-coated systems. Following this logic, the inner parallel circuit of a Warburg element W and a capacitor represent a diffusion process (W) and the double layer capacitance (C_{dl}). This is in agreement with figure 14, where semi-infinite linear diffusion is already implied in the low frequency regime.

The Warburg impedance remains well in the region of 530 to 786 nMho with a steady increase towards higher conductivities / ion concentrations. This behaviour seems plausible, since a growing supply of charge carriers implies an increasing dominance of the respective circuit element. In other words: a diffuse layer with more ions at its disposal will be accompanied by a higher voltage drop over the respective region, hence an

increased impedance.

The double layer capacitance C_{dl} lies in a range of 18.4 to 56.9 nF and shows no dependence on the conductivity.

According to Mitton et al.[24], R_f and C_f correspond to the film resistance and capacitance.

R_f shows an interesting decline over increasing conductivity with an apparent convergence towards approximately 870 Ω . The titanium oxide coating can not be considered to be a smooth homogenous layer, but has a rather rough surface, as seen in figure 13. Nor can the existence of defects from the thermal oxidation process be excluded, such as small cracks and pores. Consequently, if a large quantity of free charge carriers is available, as is the case for our sucrose and PBS solutions, one may suspect those ions to diffuse into those defects, effectively decreasing the mean electric pathway through the layer and resultingly its resistance. The close affiliation of this model circuit element with the Warburg impedance, which is used to model diffusion effects, can be argued to support this hypothesis. A stronger influence of defects, short-circuiting the passivation by a higher concentration of diffusing ions, is consistent with the similarly increasing Warburg impedance.

Following the argumentation of shortened electric pathways by diffusing ions, the steady increase in C_f from 106 nF to 150 nF can be explained similarly. In this case, the effective thickness d from $C = \epsilon_r A / d$ decreases and therefore C_f increases.

What is more, the sum of C_{dl} and C_f remains remarkably constant over all ion concentrations, as visible in table 7. One may draw the conclusion, that the increasingly dominant diffusion and double layer capacitance C_{dl} somehow assimilate the passivation capacitance C_f . On the other hand, this could as well be an indicator for further model reduction potential.

4.5 Equivalent Circuit Simulation

The model discussed in section 4.4.3 and depicted in figure 30 lays the foundation for further analysis and allows insight into state variables inaccessible to conventional measurement techniques. Such state variables include potentials and voltage drops, currents as well as absorbed powers at each respective circuit element.

4.5.1 Implementation and Simulation Setup

Equivalent Circuit Schematic:

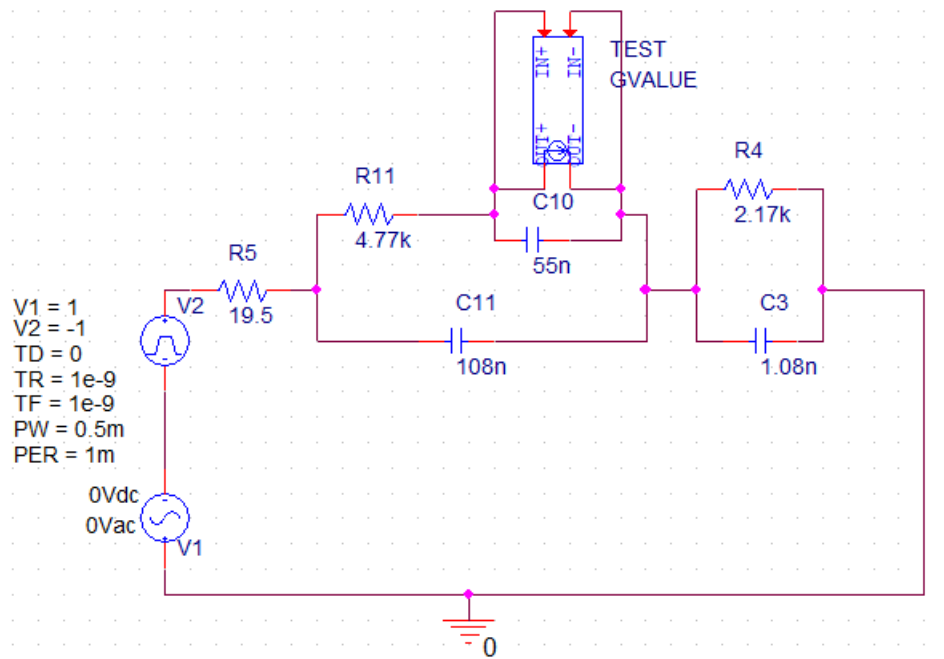


Figure 32: Implementation of the equivalent circuit for ultra-pure water in the circuit simulation software OrCAD Capture CIS[®] Lite.

The simulation of the equivalent circuit was carried out using the free circuit simulation software *OrCAD Capture CIS Lite*, as depicted in figure 32. The following elements were included and simulated using dynamic time steps of maximally 5 μs :

- *Resistors*: R4, R5 and R11 for R_e , R_p and R_f , respectively
- *Capacitors*: C3, C10 and C11 for C_e , C_{dl} and C_f , respectively
- *GValue part*: TEST GVALUE, simulating the Warburg Impedance. "[...] GVALUE parts allow an instantaneous transfer function to be written as a mathematical expression in standard notation." [31]. The used transfer function is the Warburg

Impedance's Laplace Transform and is recorded in the netlist in figure 33.

- *AC/DC Voltage Source* V1: Vdc defines the steady component and Vac the voltage amplitude of a sine signal. The frequency is defined in the *Simulation Profile*.
- *Pulse Voltage Source* V2: The parameters V1 and V2 define the upper and lower values of a trapezoidal pulse. Furthermore, there are delay time TD, rise and fall times TR and TF, pulse width PW and period length PER.

Equivalent Circuit Netlist:

```

1: * source MQ_CIRCUIT
2: V_V1      0 N73352 DC 0Vdc AC 0Vac
3: V_V2      N74786 N73352
4: +PULSE 1 -1 0 1e-9 1e-9 0.5m 1m
5: R_R4      N20842 0 2.17k TC=0,0
6: C_C3      N20842 0 1.08n IC=0 TC=0,0
7: G_TEST    N69614 N20842 LAPLACE { V(N69614,N20842) } = { PWR(s,0.5)*530n }
8: C_C10     N69614 N20842 55n TC=0,0
9: C_C11     N69969 N20842 108n TC=0,0
10: R_R11    N69969 N69614 4.77k TC=0,0
11: R_R5     N74786 N69969 19.5 TC=0,0

```

Figure 33: MilliQ equivalent circuit netlist.

A so-called *netlist* is a circuit representation in the open-source SPICE circuit description language. It defines all electronic elements and their respective connections. A netlist is the most basic representation of an electronic design in a form that is ready to be investigated by any SPICE-compatible simulation software.

Figure 33 shows an illustrative netlist for the equivalent circuit with ultra-pure water.

Simulation Profile:

The used simulation profile consisted of the standard settings with the following changes:

- Time Domain / Transient):
 - Run to time: 5 ms
 - Maximum Step Size: 5 μ s
- AC Sweep / Noise:
 - AC Sweep Type: Logarithmic Decade
 - Start Frequency: 0.1 Hz
 - End Frequency: 10^6 Hz
 - Points/Decade: 6

4.5.2 Transient Potential Drops over System Elements

In the course of the simulation runs, 28 state variables were recorded, including currents, voltages and powers for each respective circuit element. What is more, by use of the fitted values in table 7 and linear regression, circuit parameters were approximated in order to attain an estimation for equivalent circuits in a broad conductivity range. As a result, extensive data was generated using 22 circuit models, each of which representing a specific conductivity in the range of 7 to 870 $\mu\text{S}/\text{cm}$. The choice of conductivities is based on detailed experimental lysis data, which is to be merged into a predictive model of lysis rates in chapter 4.6. The following conductivities were modeled: 7, 32, 47, 50, 60, 93, 155, 160, 163, 167, 170, 174, 180, 192, 198, 230, 260, 340, 350, 440, 520 and 870 $\mu\text{S}/\text{cm}$. The simulations were conducted using a ± 1 V squared pulse as applied voltage, with a pulse length of 0.5 ms and a period duration of 1 ms.

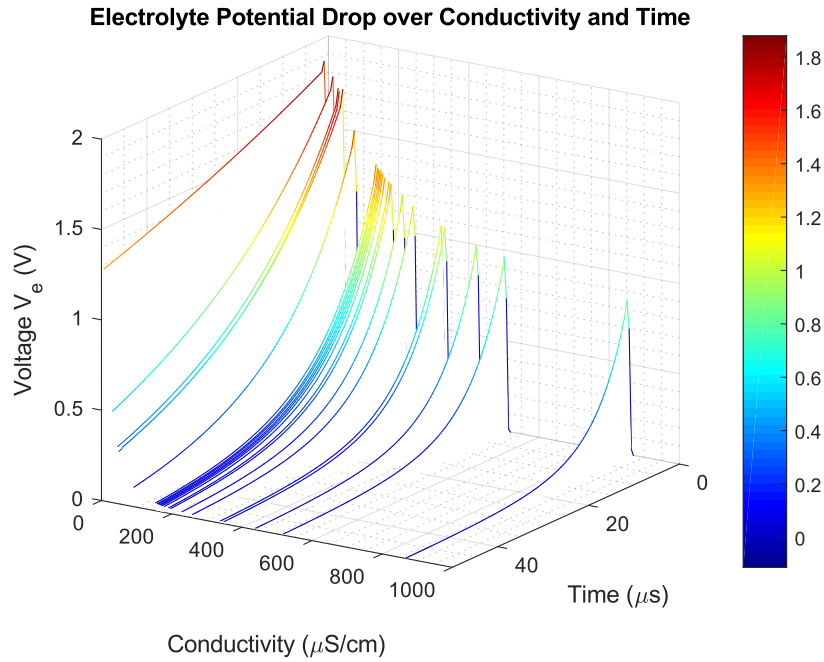


Figure 34: The simulated time-dependent electrolyte potential drop V_e over the conductivity γ .

In the following, the transient potential over the electrolyte, the Warburg Impedance as well as the nested circuit representing the titanium oxide coating will be visualized and discussed.

Figure 34 shows the time-dependent voltage drop over the electrolyte for several conductivities in the above-mentioned range. Regardless of conductivity, it shows exponential

decays, which are typical loading curves for RC-elements. With the exception of the 7 $\mu\text{S}/\text{cm}$ electrolyte, all potentials converge towards 0 V in the course of a half-period.

However, since a voltage divider is formed by the RC-element representing the electrolyte and the other parts of the circuit, we see an increase in peak voltage with rising bulk resistance (or falling conductivity). The simulated peak voltages range from 0.8 V to 1.8 V. Remarkably, for electrolyte conductivities below 400 $\mu\text{S}/\text{cm}$, peaks with a higher amplitude than the applied voltage amplitude are recorded. This is due to the voltage jump of -1 to 1 V, which leads to a ΔV of 2 V.

What is more, since the decay time $\tau = RC$ increases linearly with resistance $R = \rho l/A = l/\gamma A$, we can see a much longer exposure time of any specimen within the electrolyte to the electric field - even more so, if any lysis process takes place only above a certain voltage threshold.

We can conclude, that regulating (and increasing) the bulk resistance is a highly potent adjusting screw for controlling the lysis and transfection process.

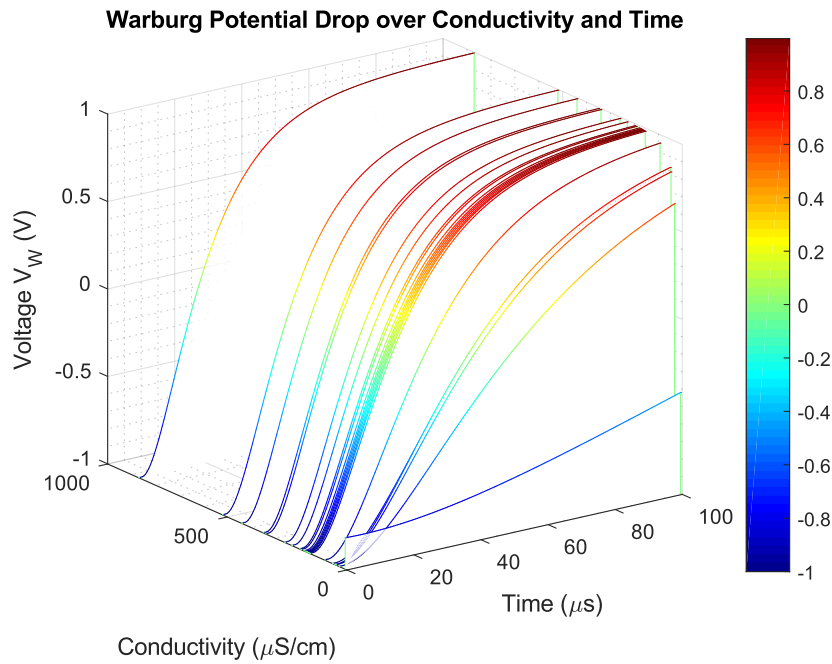


Figure 35: The simulated time-dependent potential drop over the Warburg Impedance V_W over the conductivity γ .

Figure 35 shows the transient potential drop over the Warburg Impedance. In contrast to a conventional capacitor, the Warburg element shows a step response with a continuous first derivation, leading to a smooth potential curve.

Complementary to the electrolyte potential, the potential curves converge towards ± 1 V with the exception of the conductivity of $7 \mu\text{S}/\text{cm}$, which terminates at -0.8 and 0.8 V, respectively, at the end of one half-period. For conductivities above $90 \mu\text{S}/\text{cm}$, the Warburg element approximates the terminal voltage of ± 1 V already after $50 \mu\text{s}$, effectively "shielding" the electrolyte from any applied voltage.

Next, we examine figure 36, which visualizes the potential curves over the coating/film resistance. Here, we see pulses with increasing peak values and decreasing pulse lengths over increasing conductivity. Starting and terminal values are 0 V, with the exception of $7 \mu\text{S}/\text{cm}$, which starts/ends at ∓ 0.08 V. The peak values range from approximately 0.5 V to 0.95 V.

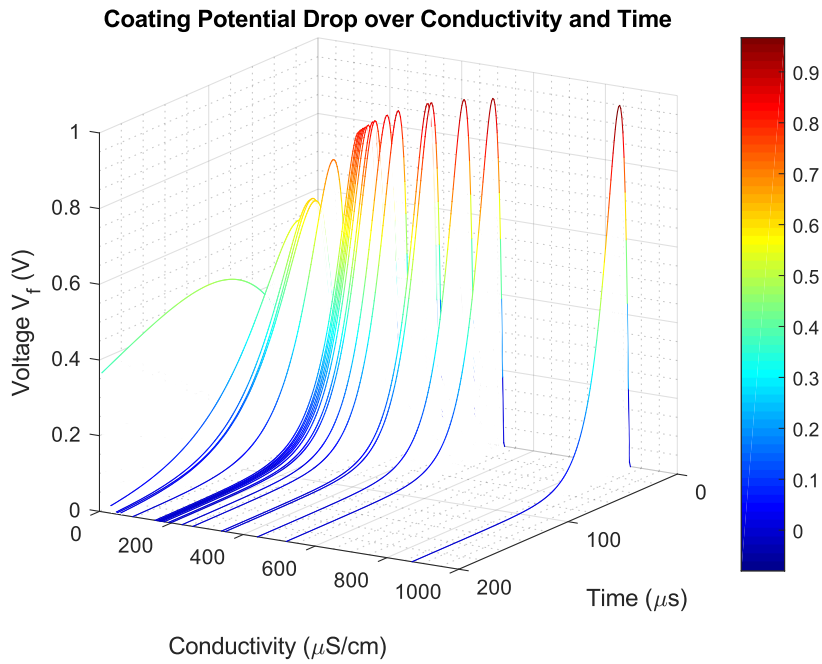


Figure 36: The simulated time-dependent film potential drop over R_f over the conductivity γ .

The large peak values at high conductivities are remarkable in that the absolute value of resistance for R_f decreases with increasing conductivity. However, the bulk resistance decreases "even faster", leading to a voltage divider with yet the bigger potential drop on the film resistance.

The increasing pulse duration $\tau_f = R_f C_f$ with decreasing conductivity can be explained by the increase in R_f , which overcompensates a decreasing C_f , as visible in table 7.

The pulse form itself, instead of a sharp exponential decay, is due to the series circuit with the W- C_{dl} -element. Their voltages add up to the voltage over C_f , which poses a

capacitive loading curve (see figure 37).

Figure 37 shows the loading curve for the coating's capacity. For conductivities above $90 \mu\text{S}/\text{cm}$, it reveals a homogeneous loading dynamic, that terminates after approximately $20 \mu\text{s}$ at 1 V . However, extremely low conductivities below $90 \mu\text{S}/\text{cm}$ associate with high R_f and therefore a longer time constant. Therefore, we see potential curves with gradually slowing loading dynamics when approaching the $7 \mu\text{S}/\text{cm}$ conductivity.

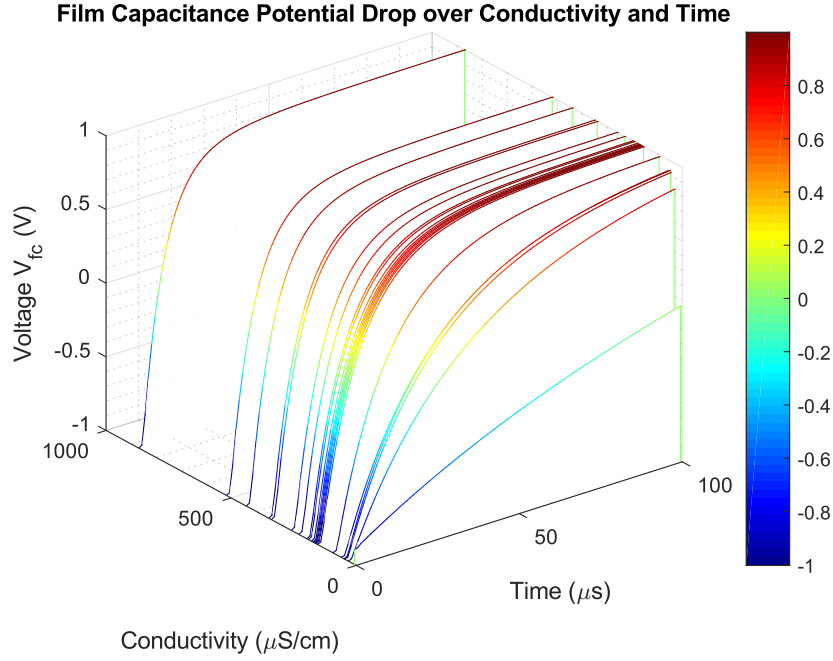


Figure 37: The simulated time-dependent film potential drop over C_f over the conductivity γ .

4.6 Statistical Lysis Model

The final goal of this Master's Thesis is to derive a statistical model for lysis rates, that incorporates all relevant parameters, such as voltage amplitudes and frequency, electric field exposure times, as well as bulk conductivity. For that purpose, access to extensive experimental lysis data was granted. This database was furthermore augmented with the simulation data extracted as described in chapter 4.5.

In the following, the strategy for unifying and adapting the empirical and simulation data will be presented.

4.6.1 Data Pooling Strategy

A fundamental hurdle for simulation-assisted statistical modeling is to find a way to efficiently create simulation data compatible with experimental features. Clearly, it is expensive or even impossible to conduct simulation runs, that cover all used permutations of lysis parameters. In our case, those were *applied voltage*, *conductivity*, *frequency* and *exposure time*. Figure 38 depicts a visualization of the composure of the experimental data. As shown, all process parameters spread over one to two orders of magnitude.

In order to reduce the number of necessary simulations, the following system characteristics were exploited.

Firstly, the equivalent circuit model of the ECMD (see chapter 4.4.2) is a linear approximation of the underlying physical processes. This is due to the electrical impedance spectroscopy measurement technique (EIS), which delivers data only by minimally disturbing the examined system, since it applies the relatively low voltage amplitude of 0.1 V. Saturation effects, if there are any, cannot be detected. Therefore, the output parameter of the derived model, namely the potential drop over the bulk electrolyte, exhibits a linear dependence on at least one of the input parameters, specifically the applied voltage. Hence, a unitary pulse of ± 1 V was used as input signal for the simulation runs. The resulting output data can easily be scaled up programmatically to experimental voltage amplitudes, e.g. ± 10 , ± 20 , ± 30 and ± 40 V.

Secondly, chapter 4.5.2 has shown, that most state variables reach a steady state after less than 100 μ seconds and converge closely towards either the applied voltage (V_{fc} , V_W) or the ground potential (V_e , V_f), especially at conductivities greater than 90 μ S/cm. In fact, all simulation setups, with the exemption of the 7 μ S/cm bulk electrolyte setup, show a steady state within one half-period of a 1 kHz input signal. What is more, as shown in figure 38, the large majority of experiments was performed at frequencies at or lower than 1 kHz. For those reasons, the simulation runs were carried out at 1 kHz. For all other frequencies, the unity step response of $V_e(t)$ was scaled to the applied voltage and multiplied with the experiment frequency and exposure time (which equals the number of pulses). That way, derived features (described in more detail in section 4.6.2), such as the time integral of the voltage curve, can be assigned to all experiments, with only

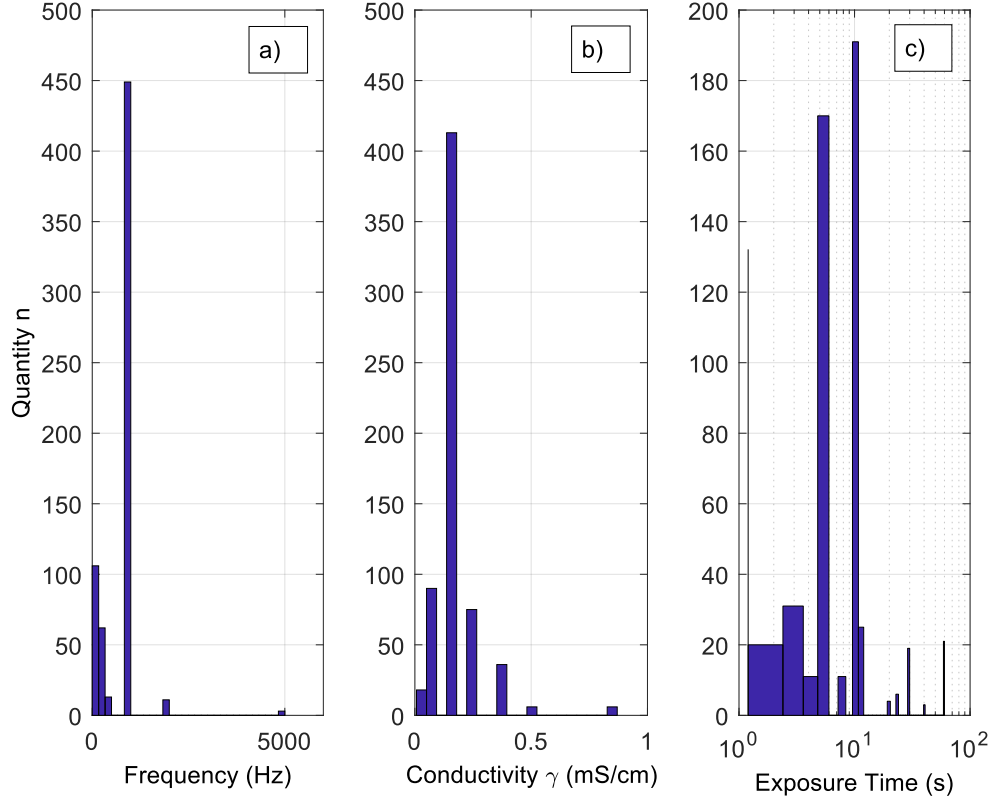


Figure 38: Histogram of experiments n over the applied frequency (a) and the used electrolyte conductivity γ (b). X-Logarithmic histogram of experiments over the applied exposure time (c).

small deviations from real values. Those deviations are particularly low for the majority of experiments that were taken at conductivities greater than $50 \mu\text{S/cm}$.

Thirdly, the parameter *conductivity* was considered. However, contrary to the aforementioned process parameters, changing the electrolyte conductivity severely affects the system characteristics and behaviour. Furthermore, it cannot be simply changed with the input signal. As a result, it was necessary to realize this feature in 23 separate simulation setups as different equivalent circuits, customized to every occurring conductivity in the database. Manual simulation runs were conducted and the respective step responses saved as files in the csv-format. Thereon, all data was ready to be processed for the generation of derived features, subsequent data point complementation and, eventually, automated model building.

4.6.2 Derived Features and Augmentation

In the following section, the additional features derived from the raw simulation data will be presented and discussed.

Experimental	Derived
Lysis Rate	PeakVoltage
Voltage	AuCVoltage
Conductivity	AuCVoltageCut
Frequency	Tau
Exposure Time	PeakPower
-	AuCPower

Table 8: Lineup of experimental parameters and derived variables, which build a new data point.

PeakVoltage: PeakVoltage represents the peak value of the $V_e(t)$ potential curve.

AuCVoltage: AuCVoltage stands for *Area under Curve* and represents the time integral of $V_e(t)$. In order to account for different frequencies and exposure times, AuCVoltage is multiplied with the resulting pulse number, as in

$$AuCVoltage = \int_{t_0}^{t_1} V_e(t) dt \cdot f \cdot t_e \quad (4.10)$$

with t_0 and t_1 being the starting and end time of the simulated half period, f the frequency and t_e the exposure time.

AuCVoltageCut: AuCVoltageCut describes the time integral of $V_e(t)$ above a certain threshold. Lysis and transfection data suggests, that those processes occur only, if a certain critical electric field strength within the bulk electrolyte is surpassed. For an exponential decay, the resulting area can be calculated as

$$AuCVoltageCut = (-P\tau \left(\frac{S}{P} - 1\right) + S\tau \ln \frac{S}{P}) \cdot f \cdot t_e \quad (4.11)$$

with the voltage peak value P , the arbitrary threshold S , pulse time constant $\tau = R_e/C_e$, frequency f and exposure time t_e .

Tau: Tau represents the characteristic time of the R_eC_e -element. It can be calculated either directly with the known values for R_e and C_e or by taking the subsequent slope k at the peak value V_p of the exponentially decaying pulse and reformulating, such as $\tau = V_p/k$.

PeakPower: PeakPower represents the peak value of the ohmic power losses in the electrolyte.

AuCPower: AuCPower represents the time integral of the resistive losses and therefore the overall energy that dissipated in the electrolyte during the experiment. It is calculated as

$$AuCPower = \int_{t_0}^{t_1} P_e(t) dt f t_e \quad (4.12)$$

with t_0 and t_1 being the starting and end time of the simulated half period, $P_e(t)$ the resistive power losses, f the frequency and t_e the exposure time.

Data point complementaion was achieved simply by calculation of the additional features and subsequent concatenation to the data table.

4.6.3 Data Exploration

Data scientists can choose from miscellaneous statistical methods or machine learning algorithms to build predictive models, e.g. (non-)linear regression models, random forests or neural networks. To make an optimal decision, deep expertise is often required. However, sometimes the nature of the fundamental data follows a clear pattern, that points in a very distinct direction. Figure 39 gives an example for the revelation capabilities of exploratory data science.

Figure 39 shows a cleaned subset of the experimental lysis rates over the applied voltage. The data is composed of numerous experimental series, in which the applied voltage is increased step-wise from 0 to 40 V with otherwise fixed parameters, such as the electrolyte conductivity, frequency and exposure time. The subset of data, that fulfills this precondition of consecutiveness, is plotted in figure 39 as blue dots. For illustration, spline interpolations were created for each such run, drawn in red.

The lysis rate follows a distinct sigmoid curve over the applied voltage. Naturally, this curve starts out with 0% lysis rate at 0 V, then gradually increases after surpassing a certain threshold voltage between 7 and 15 V and eventually converges towards 80 to 100% between 20 to 30 V, for most experiments. Furthermore, this sigmoidal course shows two distinct features. Firstly, it seems to shift in the x-direction, following a hidden parameter invisible in this 2D visualization. Secondly, the maximum steepness at intermediate voltages seems to be a rather universal characteristic.

One can draw the conclusion, that the lysis process sets in only after a certain threshold voltage is surpassed. Furthermore, cells show greatest voltage sensitivity at intermediate voltages (when the steepness is at its maximum). Self-explanatory, cell lysis rates can not exceed 100%.

From a model building perspective, the lysis rates pose the so-called *response variable*. Given our specific input variables, as described in table 8, the lysis rates shall be predicted. As visible in figure 39, the lysis rates are subject to a number of rules, which are to be wisely exploited. First and foremost, the lysis rates rise monotonously and

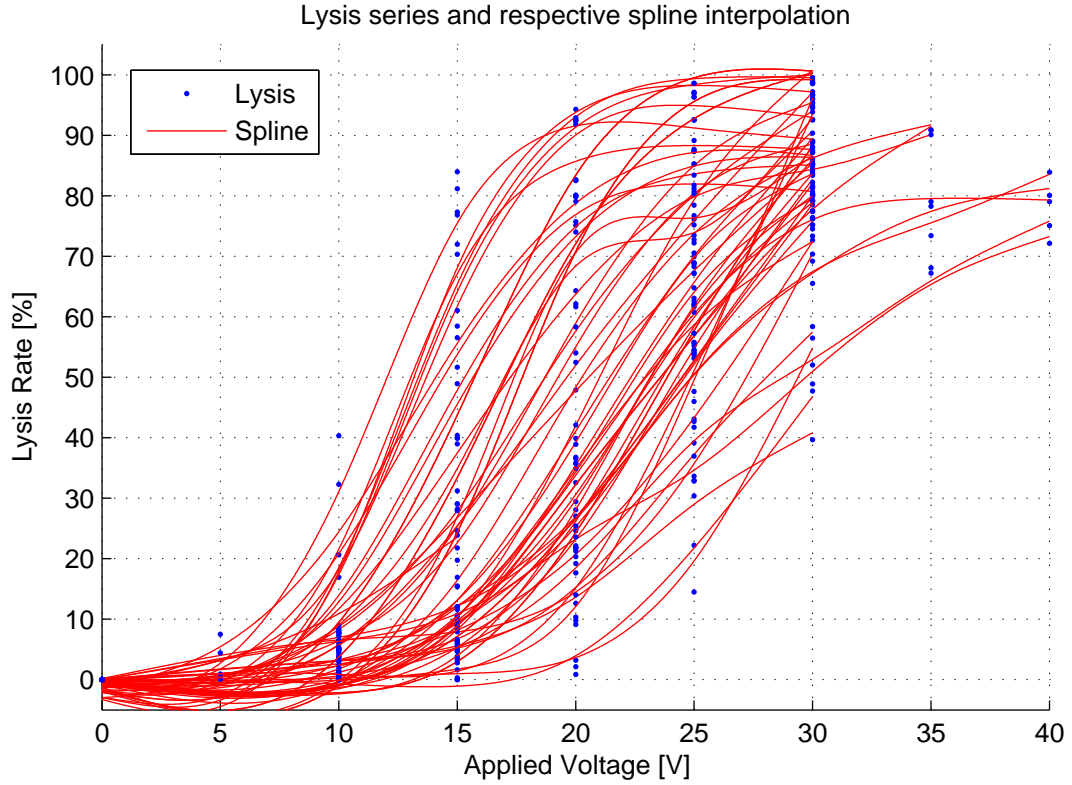


Figure 39: Experimental HEK cell lysis series and spline interpolation.

steadily, which advises a regression model as modeling approach. However, we see a clear non-linear pattern in the form of a sigmoidal curve. What is more, we have logical boundary conditions for the lysis rates, which are 0% and 100%, trivially. Therefore, all linear regression models can be excluded - we can not expect the only non-linear input variables AuCVoltage and AuCPower to do the trick on their own.

As a result, a method is proposed and tested, which unites both typical advantages of regression models, such as innate interpolation capability and frugality towards available processing power, as well as the ability to categorize data: *Multinomial Logistic Regression*.

4.6.4 Multinomial Logistic Regression Model

Multinomial logistic regression is a classification method to predict "[...] categorical placement in or the probability of category membership" [30] of a response variable on one or more input variables (features). The response variable can either be binary (dichotomous), like the distinction between male and female, polytomous, like preferred

products to buy, or continuous, like levels of severity of disease or *lysis rates*. If there is a natural order among these responses, they are called *ordinal* and if not, *nominal*. The application of Multinomial Logistic Regression is attractive and common, since it "[...] does not assume normality, linearity or homoscedasticity" [30].

For our purposes the Matlab[®] *Statistics and Machine Learning Toolbox*[®] function *mnrfit()* was used. Firstly, we create an ordinal response variable by sorting the continuous target variable 'lysis rate' into 20 equidistant intervals of $\Delta d_i = 5\%$. Next, we hand over the fitting parameters:

- $m \times n$ input matrix X (as described in table 8, m number of data points, n number of input variables)
- Ordinal Response Variable (empirical lysis rates)
- Response Variable Type ('ordinal')
- Link Function ('loglog')

Subsequently, *mnrfit()* returns a matrix B of coefficient estimates for a multinomial logistic regression of the ordinal responses, as well as the deviance of the fit, dev, and stats, which includes model statistics such as standard errors for coefficient estimates, degrees of freedom and residuals.

Next, we use the respective predictive function *mnrval()* to gain an estimate of probabilities for each lysis rate interval for a given lysis experiment (= input variables). For example, if we hand over a 1×10 input matrix (Voltage, Exposure Time, Frequency, Conductivity, PeakVoltage, AuCVoltage, AuCVoltageCut, PeakPower, AuCPower, τ) and want to predict the corresponding lysis rate, *mnrval()* will return a 1×20 matrix *pihat*, which contains 20 probabilities for the respective lysis rate interval defined in the ordinal response variable. Furthermore, *mnrval()* provides the lower and upper 95% confidence interval for each probability.

Consequently, if one seeks to gain an estimate for the lysis rates, the most robust way is to calculate the predictand,

$$E(Lysis) = \sum_{i=1}^{20} p_i d_i. \quad (4.13)$$

In the same manner, the 1σ or 2σ confidence intervals can be calculated by creating a cumulative sum of probabilities. The respective cumulative probability threshold (32% and 68% or 5% and 95%) marks the lysis rate intervals, which correspond to the lower and upper bounds of the confidence intervals.

4.6.5 Model Performance

In the following, the results and performance of the derived ordinal multinomial logistic regression model (as described in chapter 4.6.4) will be elucidated. Figure 40 provides a visual overview of the model's classifications. Predictive lysis curves are created for three different conductivities, $\gamma = [93, 260, 360] \mu\text{S}/\text{cm}$. Error bars are plotted for the 1σ confidence interval, meaning that 68% of lysis data lies within the specified range.

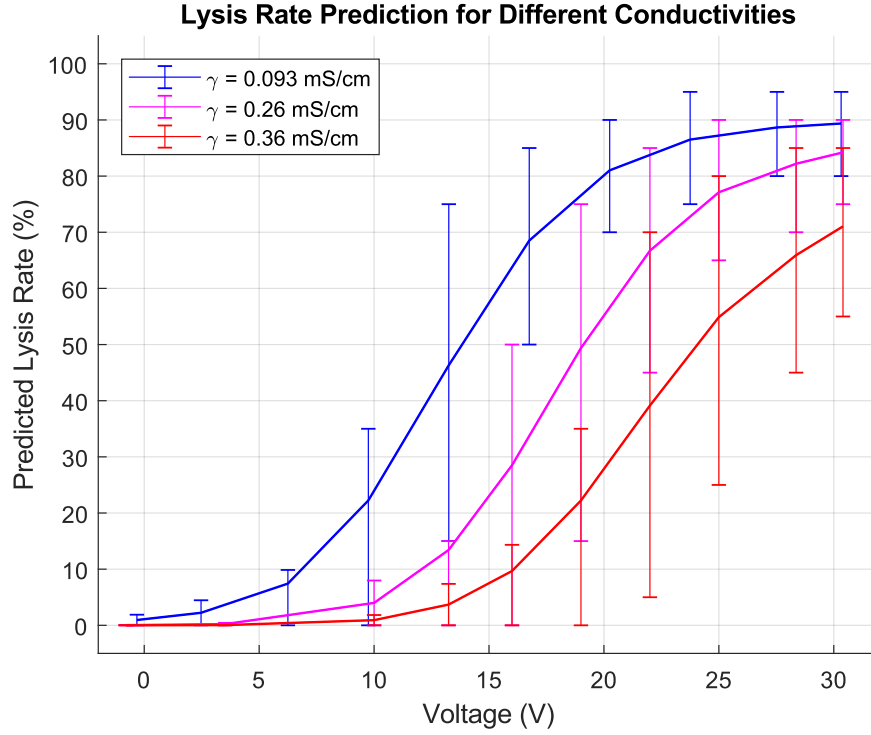


Figure 40: Predicted lysis rates by multinomial logistic regression for different conductivities γ . Confidence intervals are plotted for 1σ , signaling that 68% of lysis experiments lie within the specified range.

Firstly and foremost, we see a clear distinction in lysis curves between different conductivities: the higher the conductivity, the greater the need for higher voltages. This is consistent with the experimental data and also with the considerations about the voltage drop across the bulk electrolyte, which is proportional to the local electric field strength and to the bulk resistance.

Secondly, the desired sigmoidal curves are realized, with the boundary conditions of 0% and 100% and the steady and monotonous increase in lysis rate over the applied voltage.

Thirdly, the error bars reveal strong uncertainties, especially in those regions, where cells are the most sensitive to increases in applied voltage. In other words, the confidence

intervals become broader with the steepness of the predicted lysis curve. This is emphasized by figure 41, which compares the confidence interval broadness with the respective steepness and suggests a clear correlation. These uncertainties originate from two major factors: Firstly, lysis experiments inherently show great statistical variance. Single experiments can show up to $\pm 15\%$ scattering under seemingly equivalent laboratory conditions. This might be due to unavoidable imprecisions in the handmade ECMDs (electrical cell manipulation device) and individual variations in every cell passage used for experiments. Furthermore, optical evaluations of cell lysis rates are also prone to small divergences. Secondly, ordinal multinomial logistic regression, while demonstrating that cell lysis prediction can be done, might not be the best statistical approach for predictive analysis in this very case. Therefore, we can assume that a significant part of uncertainty is also introduced by the used machine learning approach, which leaves room for optimization. For example, the introduction of lysis rate intervals d_i creates quantization noise, when used for accuracy analysis (see figure 41). However, a final and thorough investigation of a reasonable set of possible algorithms and their accuracies would go beyond the scope of this thesis.

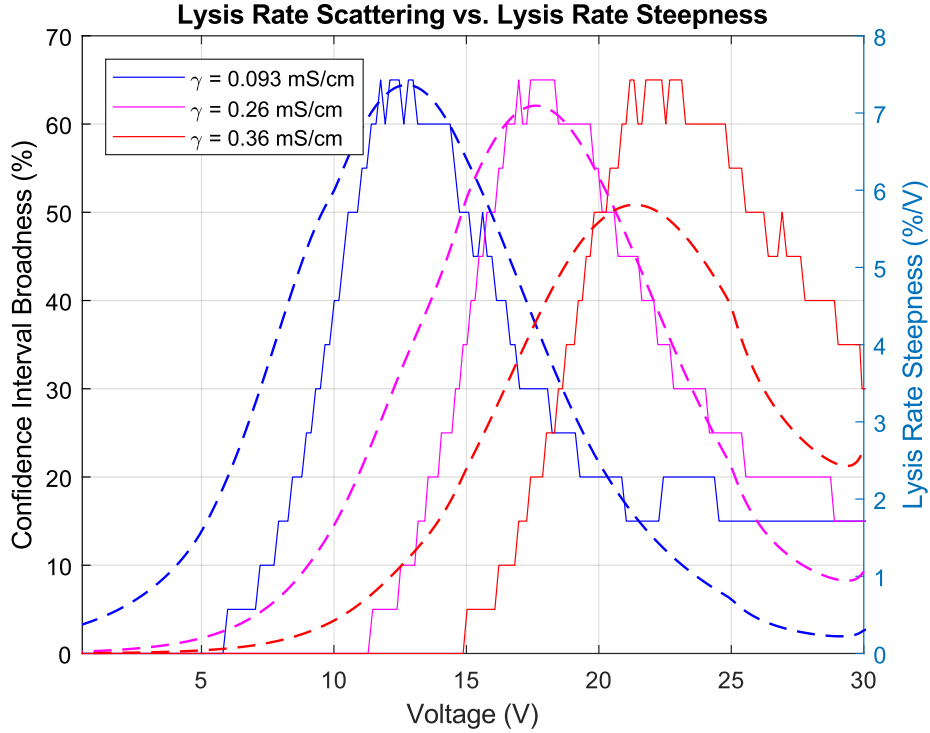


Figure 41: Broadness of the 1σ confidence interval over the applied voltage, depicted as solid lines. Confidence intervals correlate strongly with the lysis curve steepness, which are plotted as dashed lines.

Model Verification

In the following, the predictive power of the model will be assessed and verified by comparing its prediction with empiric lysis values of a HEK cell line. The test features are only composed of the frequency, exposure time, applied voltage and conductivity, which represent the available standard process parameters of a cell lysis experiment. However, neither combination of those parameters was included in the training data - thus it will be interesting to examine the performance under those "difficult" conditions.

The control experiments were conducted using symmetric squared pulses and the parameters depicted in table 9.

Conductivity	Frequency	Applied Voltage	Exposure Time
210 $\mu\text{S}/\text{cm}$	1 kHz	25 V	3 s
210 $\mu\text{S}/\text{cm}$	5 kHz	15 V	1.2 s
210 $\mu\text{S}/\text{cm}$	1 kHz	18 V	6 s
210 $\mu\text{S}/\text{cm}$	1 kHz	35 V	0.1 s

Table 9: Verification experiment parameters. In total, four different experiments were conducted, which were repeated three times each.

Figure 42 provides an illustration for the resulting prediction compared to the empirical values for four different experiments, which were repeated three times, respectively. Note that the conductivity of 210 $\mu\text{S}/\text{cm}$ was not included in the training set.

Firstly, we observe that all empirical data points remain well within the 1σ (68%) confidence interval for lysis rate predictions. Secondly, a distinct over-estimation is visible for experiments with a comparatively large number of pulse passages ($1.2 \text{ s} * 5 \text{ kHz} = 6000$ pulses for experiment 2 and $6 \text{ s} * 1 \text{ kHz} = 6000$ pulses for experiment 3). This indicates a reliance of the model on accumulation effects, which seem to be less profound in laboratory experiments. Moreover, the voltages 15 V and 18 V lie exactly in a region, where lysis training data itself shows the most pronounced uncertainty, as visible in figure 40. Thirdly, this trend reverses in case of large applied voltages (25 V for experiments 1 and 35 V for experiment 4), where predictions show a slight tendency to underestimate lysis rates.

Conclusively, with regard to the inherent biological scattering and our restriction to only one model to process numerous parameters, which stretch over several orders of magnitude each, we may infer satisfactory predictive performance.

4.6.6 Cell Lysis Threshold Voltage / Electric Field Strength

The motivation that perpetuates this entire master's thesis is to find out the threshold electric field strength for cell lysis locally at the specimen. For this purpose, naturally,

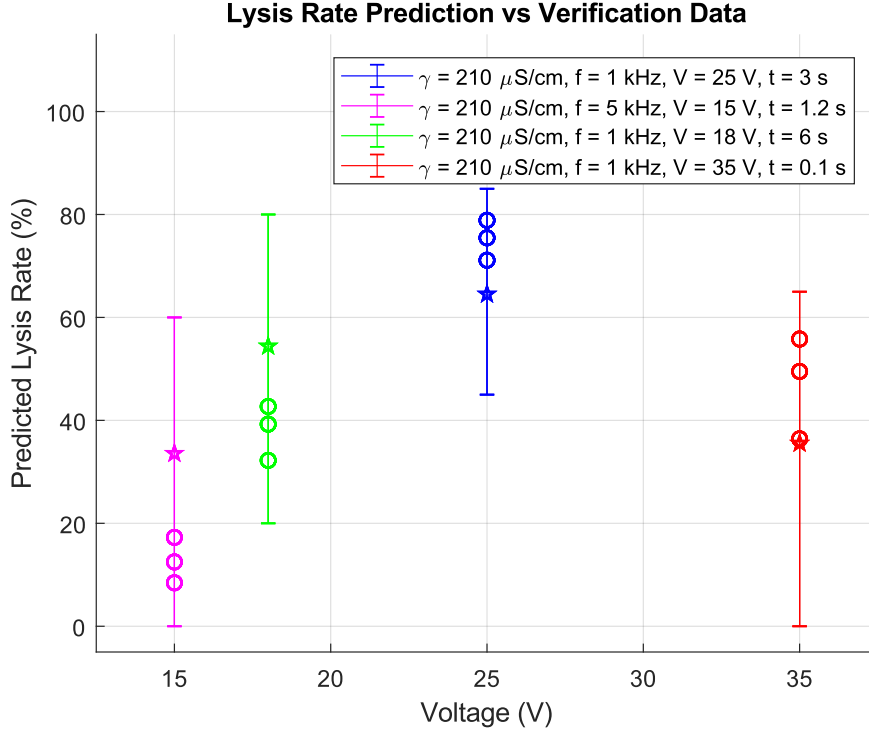


Figure 42: Bar plot representing the 1σ prediction confidence interval. Four experiments were conducted for verification with three repetitions each (circle marks). Each respective lysis rate prediction value is marked as a star.

it is necessary to estimate the intrafluidal local electric field strength, which, in theory, can be calculated using the potential drop $\Delta\varphi$ over a path d in

$$\vec{E}_{local} = -\frac{\Delta\varphi}{d} \quad (4.14)$$

with \vec{E}_{local} as local electric field strength, $\Delta\varphi$ as potential drop over the electrolyte and d as the length of the electric path through the electrolyte. However, this simple method can not trivially be applied to an electrolyte between two electrodes, since it neglects potential drops induced by double layer capacities. What is more, if the electrodes are equipped with a coating, as in our case, the effective potential drop over the homogeneous electrolyte becomes an utter mystery, since the coating itself usually shows complex electric behaviour.

Nonetheless, thanks to the electric equivalent circuit model from chapter 4.4.2, our simulations from chapter 4.5.2 and our extensive empirical data, we can place our derivations on a sound basis and make transparent assertions.

In the following, a key prediction feature for lysis rates will be presented. Subsequently, the advantage of utilizing certain simulation data will be shown by contrasting it to the

simple method of dividing the applied voltage by the electrode distance in equation 4.14 with $\Delta\varphi = V_{\text{applied}}$, to attain a value for the threshold electric field strength.

There is no firm convention for defining a lysis threshold field strength. It seems reasonable, to define the threshold field strength as the value, at which there is a 50% chance to lyse a certain specimen. This definition is equivalent to the electric field strength, at which a 50% lysis rate is achieved.

Following this definition, figures 43 and 44 illustrate at which combination of conductivity and applied voltage/peak voltage the lysis rate reaches 50%. In other words, each data point (blue circles) represents a lysis experiment, where the resulting lysis rate was 50% and it is located at the used conductivity and voltage values.

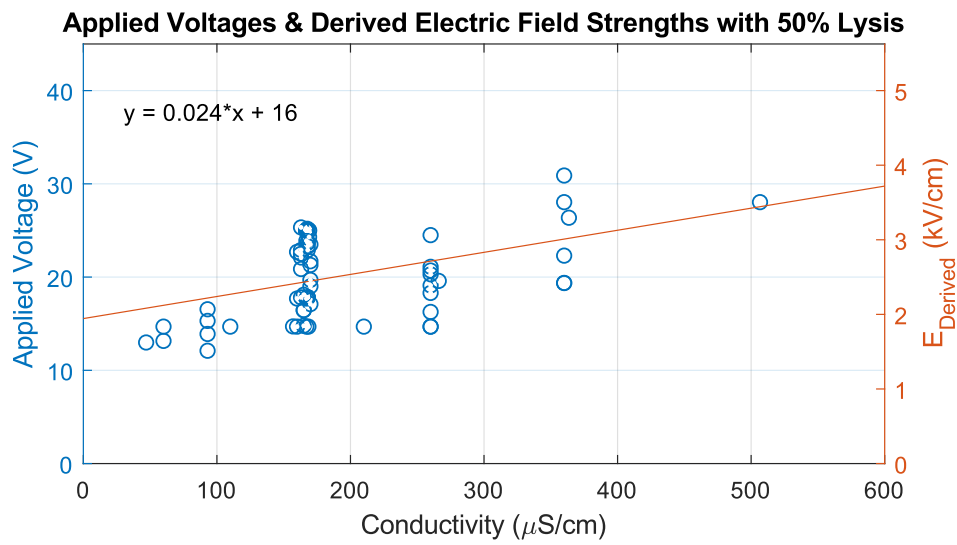


Figure 43: HEK cell lysis experiments that yield 50% lysis rates (blue circles) over conductivity and the applied voltage on the system. A linear regression (orange line) of the scatter plot indicates a significant dependence of the necessary applied voltage on the conductivity.

Figure 43 shows the lysis experiment in dependence on the applied voltage on the system. This value is known to the person conducting the experiment. One may be tempted to use this information for deriving a local electric field strength as in equation 4.14, but this would lead to sloppy results, since the electrical dynamics of the system were neglected, as discussed above. This pitfall is visible in figure 43 as a scatter plot with a clear skew to the upper right, as the respective linear regression emphasizes. The need to apply higher voltages with increasing conductivity comes from the fact, that our system creates a voltage divider over the electrode coating and the electrolyte. Since the resistance of the electrolyte decreases with increasing conductivity, the relative voltage drop and resulting electric field strength within the electrolyte decrease as well. This

needs to be compensated by higher applied voltages.

If a threshold value for lysis rates was to be extracted by means of only the applied voltage and geometrical considerations (and the occurrence of significant errors at low and high conductivities was ignored), the resulting mean electric field strength for a 50% lysis rate with HEK cells was 2.48 kV/cm and occurred at an applied voltage of 20.13 V.

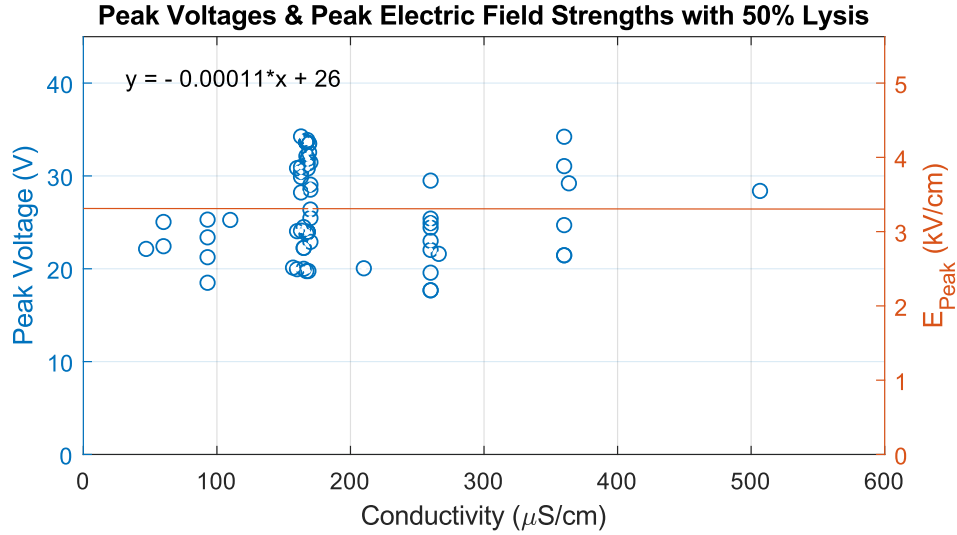


Figure 44: HEK cell lysis experiments that yield 50% lysis rates (blue circles) over conductivity and the peak value of the transient voltage drop within the electrolyte. A linear regression (orange line) of the scatter plot indicates that the peak voltage leading to 50% lysis is independent from the electrolyte conductivity.

Finally, a more reliable and relevant feature to assess the desired threshold electric field strength will be introduced in the following. Our electric equivalent circuit model from chapter 4.4.2 and the subsequent simulations from chapter 4.5.2 allow us to separate the electrolyte from the embedding system. As a result, we can describe the transient voltage drop over the electrolyte more precisely. It makes sense to define the threshold electric field strength on the basis of a feature, that is less dependent on the conductivity.

In this manner, figure 44 illustrates lysis experiments, where a 50% lysis rate was achieved, over the conductivity and the *peak voltage* of the time-dependent voltage drop over the electrolyte. In contrast to figure 43, a closer look at the linear regression equation reveals that the slope coefficient is close to zero, indicating that the peak voltage for a 50% lysis rate is independent from the conductivity. The above-mentioned voltage divider and adjacent dynamic effects within the coating are accounted for. This means, that the electrolytic voltage drop is isolated and its effect on lysis can be studied with fewer obfuscating effects.

The peak voltage drop within the electrolyte seems to have universal validity over all conductivities. Therefore, it is a good candidate for introducing a threshold electric field strength. The mean peak voltage that leads to a 50% lysis rate with HEK cells is 26.47 V, which translates to a local electric field strength peak of 3.27 kV/cm. This value is in good agreement with, for example, Rosazza et al., who state, that the threshold field strength for electroporation " [...] for eukaryotic cells, (diameter between 10 μm and 30 μm), is close to 1000 V/cm and for bacteria [...] in the order of 6000 V/cm" [8]. Since electroporation poses the preliminary stage for electrolysis, a cell *lysis* threshold for human HEK-293 cells, with a diameter of 11-15 μm [33], of approximately 3 kV/cm seems reasonable.

5 Conclusion

In 2016, a novel and promising microfluidic electric device was presented by Wassermann et al. at AIT Austrian Institute of Technology, which proved effective for cell specific lysis. On the basis of this technology, specific lysis of blood cells in a mixture with bacteria was shown[27]. Furthermore, it was demonstrated in 2017, that lysis specificity could be enhanced to the level of successful distinction between healthy donor leukocytes and leukemic Jurkat T cells[29].

The aim of this thesis was to characterize this technology from an electrical engineering perspective, form a model to gain insight into process variables, first and foremost about the actual electric field strength specimen are subjected to, and eventually create a predictive model for lysis rates, that incorporates all process parameters at hand.

Key elements of this technology are, firstly, the spatial dimensions, which allow for finely tunable electrical field strengths in the kV/cm range with applied voltages of below 40 V and, secondly, the electrode passivation layer. This coating, which consists of high- κ -dielectric titanium oxide, functions as a galvanic barrier between the metal electrodes and the electrolyte.

It was shown, that the titanium oxide is not a passive electrical component, but forms a Schottky diode in the system due to its n-type semiconductor characteristic. The resulting diode characteristic was quantified by using a manual DC measurement procedure. Moreover, a measurement setup was devised to retrieve information about the resulting transient intra-fluidal potential profile created by the electrode-passivation-electrolyte interface. As a result, high resolution, multi-channel data could be generated. Consequently, a clear rectification effect of the electrolyte potential profile could be determined and its manifestation and frequency dependence investigated.

Furthermore, an electrical equivalent circuit model for the overall system was generated on the basis of a set of electrical impedance spectroscopies (EIS). The resulting model is based on the *coated metal model* and allows for the consideration of all process variables at play, such as applied voltage, used electrolyte conductivity, frequency, exposure time and pulse shape of the applied signal. As a result, multiple state variables, including the voltage drop over the electrolyte, are made accessible in a time and frequency domain and their dependence on individual process variables can be determined.

Hereafter, a multinomial regression model for lysis rate prediction was established. For that purpose, in addition to empirical data including the standard process parameters, derived features from the equivalent circuit simulation were created and a data unification strategy developed and implemented. Consequently, the feasibility of a predictive model for lysis rates with reasonable confidence intervals and sensitivity to key process parameters could be shown. Subsequently, the model's performance was assessed by comparing predictions with respective lysis experiments with highly diverse process parameters.

5.1 Outlook

A significant improvement potential for the ECMD project lies in lifting the production and cell lysis processes out of the manual stage into the industrial automated stage. Sensitive design parameters, such as the distance between the plan-parallel electrodes, as well as thickness, homogeneity and integrity of the oxide layer could be controlled more conveniently, reliably and continuously. Besides truly replicable device parameters, lysis data would also become more stable and subsequently more precise models could be derived.

The introduced lysis rate prediction model is a small demonstration of how rapidly results can be achieved with modern machine-learning approaches. However, due to the highly multi-variate nature of our problem statement, additional empirical data is necessary to generate more precise and reliable models. In the future, as cell-specific lysis has already been demonstrated by Wassermann et al.[27], it is plausible to extend the model to be able to make predictions for multiple cell types and thus eventually allow researchers or medical staff to eliminate arbitrary subsets of specimen from a cell sample suspension.

The application of electric fields to biological samples promises high potential in the fields of biotechnology and medicine. By galvanic decoupling of the electrolyte and electrodes, the ECMD project achieved a more controllable exposure of cells to electric fields[27]. In the course of this thesis, the foundation was laid for a deeper understanding of the inner workings of the ECMD and novel insights about the transient electric field strength within the electrolyte were gained. These results may initiate further innovation by providing new input for better designs. As the research field is still dominated by missing standardization and contradicting findings, hopefully, this contribution helps to unlock the potential of this electroporation and cell specific lysis technology.

References

- [1] Hine, Robert; *The Facts on File Dictionary of Biology*; 3rd ed. New York: Checkmark, 1999: 198; ISBN-13: 978-0816039081.
- [2] Mary Louise Turgeon; *Clinical Hematology: Theory and Procedures.*; Lippincott Williams & Wilkins; p. 100; 2004; ISBN: 9780781750073.
- [3] Pauly H, Schwan HP; *Über die Impedanz einer Suspension von kugelförmigen Teilchen mit einer Schale.*; Z Naturforsch B 14:125–131; 1959.
- [4] Kotnik, Tadej; Pucihar, G.; *Induced Transmembrane Voltage - Theory, Modeling, and Experiments.*; Journal of Membrane Biology; 2010; DOI: 10.1007/s00232-010-9279-9.
- [5] Stephen H Wright; *Generation of resting membrane potential*; Advances in Physiology Education 28:139-142; 2004; DOI:10.1152/advan.00029.2004.
- [6] Cheng, K; Haspel, HC; Vallano, ML; Osotimehin, B; Sonenberg, M; *Measurement of membrane potentials (psi) of erythrocytes and white adipocytes by the accumulation of triphenylmethylphosphonium cation*; J. Membr. Biol. 56 (3): 191–201.; 1980; DOI:10.1007/bf01869476.
- [7] Lo, CJ; Leake, MC; Pilizota, T; Berry, RM.; *Nonequivalence of membrane voltage and ion-gradient as driving forces for the bacterial flagellar motor at low load*; Biophys J. 2007 Jul 1 93(1):294-302. p.295; DOI: 10.1529/biophysj.106.095265.
- [8] Rosazza, Christelle; Haberl Meglic, Sasa; Zumbusch, Andreas; Rols, Marie-Pierre; Miklavcic, Damijan; *Gene Electrotransfer: A Mechanistic Perspective*; Current Gene Therapy, 2016, 16, 98-129; DOI: 10.2174/1566523216666160331130040.
- [9] Hermann von Helmholtz; *Studien über electrische Grenzsichten.* In: G. Wiedemann (Hrsg.): Annalen der Physik und Chemie. Band 243, Nr. 7. Verlag von Johann Ambrosius Barth, Leipzig 1879, S. 337–382; DOI: 10.1002/andp.18792430702.
- [10] Bard, A. J.; Faulkner, L. R; *Electrochemical methods: Fundamentals and applications.*; New York: Wiley; 2001; ISBN 13: 9780471043720.
- [11] Grimnes, S.; Martinsen, O.G.; *Bioimpedance and bioelectricity basics*; Academic Press; 2000; ISBN: 9780123032607.
- [12] Stern, O. Z.; Electrochem, 30, 508; 1924.
- [13] L. Sharma, Ed.; *Metal-Semiconductor Schottky Barrier Junctions and Their Applications.* New York, NY: Plenum; 1984; ISBN 978-1-4684-4655-5.
- [14] Lvovich, V. F.; *Impedance Spectroscopy: Applications to Electrochemical and Dielectric Phenomena*; Wiley: Somerset, NJ, USA; 2012; ISBN: 978-0-470-62778-5.

- [15] Hirschorn, Bryan; Orazem, Mark E.; Tribollet, Bernard; Vivier, Vincent; Frateur, Isabelle; Musiani, Marco; *Constant-Phase-Element Behavior Caused by Resistivity Distributions in Films*; Journal of The Electrochemical Society, 157 (12) C452-C457; 2010; DOI: 10.1149/1.3499564.
- [16] Krause, S.; *Impedance methods* in Encyclopedia of Electrochemistry; A. J. Bard (Ed.), Wiley-VCH, Vol. 3; 2001; ISBN: 9783527303953 3527303952.
- [17] Bard, A. J.; Faulkner, L. R.; *Electrochemical Methods: Fundamentals and Applications*; 2nd ed.; John Wiley & Sons, Inc.: New York; 2001; ISBN 13: 978-0471043720.
- [18] Randles, J. E. B.; *Kinetics of rapid electrode reactions*. Discussions of the Faraday Society. 1: 11.; ISSN 0366-9033.; 1947; DOI: 10.1039/df9470100011.
- [19] Ritesh N. Vyas; Kuyen Li; Bin Wang; *Modifying Randles Circuit for Analysis of Polyoxometalate Layer-by-Layer Films*; J. Phys. Chem. B, 114 (48), pp 15818–15824; 2010; DOI: 10.1021/jp105075t.
- [20] Feliu, V.; González, J.A.; Adrade, C.; Feliu, S.; *Equivalent circuit for modelling the steel-concrete interface. II. Complications in applying the stern-geary equation to corrosion rate determinations*; Corrosion Science, Volume 40, Issue 6, p 995-1006; 1998; DOI: 10.1016/S0010-938X(98)00037-7.
- [21] Andreaus, B.; McEvoy, A.; Scherer, G.; *Analysis of performance losses in polymer electrolyte fuel cells at high current densities by impedance spectroscopy*; Electrochimica Acta, Volume 47, Issues 13-14, p 2223-2229; 2002; DOI: 10.1016/S0013-4686(02)00059-2.
- [22] Palraj, Sironmani; Selvaraj, Muthaiah; Muthukrishnan, Sundarajan; *Effect of pre-treatments on electrodeposited epoxy coatings for electronic industries*; AIMS Materials Science, 3(1): 214-230.; 2016; DOI: 10.3934/matricsci.2016.1.214.
- [23] S. Duval, Y. Camberlin, M. Glotin, M. Keddam, F. Ropital, H. Takenouti; *Characterisation of organic coatings in sour media and influence of polymer structure on corrosion performance*; Progress in Organic Coatings 39, p 15–22; 2000; DOI: 10.1016/S0300-9440(00)00094-1.
- [24] D. B. Mitton, S. L. Wallace, a N. J. Cantini, a F. Bellucci, G. E. Thompson, N. Eliaz and R. M. Latanisiona; *The Correlation Between Substrate Mass Loss and Electrochemical Impedance Spectroscopy Data for a Polymer-Coated Metal*; Journal of The Electrochemical Society; 2000; DOI: 10.1149/1.1473777.
- [25] Sonja Kirsch, Rainer Bockmann; *Membrane pore formation in atomistic and coarse-grained simulations.*; Biochimica et biophysica acta 1858 (10), pp. 2266–2277; 2016; DOI: 10.1016/j.bbamem.2015.12.031.
- [26] Benjamin J. Morgan, Graeme W. Watson; *Intrinsic n-type Defect Formation in TiO₂: A Comparison of Rutile and Anatase from GGA+U Calculations*; J. Phys. Chem. C, 114, 2321–2328; 2010; DOI: 10.1021/jp9088047.

- [27] Wassermann KJ, Barth S, Keplinger F, Noehammer C, Peham JR; *High-k Dielectric Passivation: Novel Considerations Enabling Cell Specific Lysis Induced by Electric Fields.*; ACS Applied Materials & Interfaces, 8(33):21228-35.; 2016; DOI: 10.1021/acsami.6b06927.
- [28] Eberhard Neumann, Sergej Kakorin, Katja Toensing; *Principles of Membrane Electroporation and Transport of Macromolecules*; Methods in Molecular Medicine, Vol. 37: Electrically Mediated Delivery of Molecules to Cells; 2000; DOI: 10.1385/1-59259-080-2:1.
- [29] Köhler, Verena; *Electrical Cell-Specific Lysis for Rapid Biomarker Detection from Complex Biological Samples Using a Microfluidic Device.*; 2017; Master Thesis; Institute for Biotechnology, University of Natural Resources and Life Sciences, Vienna.
- [30] J. Starkweather, A. Moske; *Multinomial Logistic Regression*; 2011; available at https://it.unt.edu/sites/default/files/mlr_jds_aug2011.pdf [accessed Sept. 27th, 2018]
- [31] Cadence Design Systems, Inc.; *PSPice®: User's Guide*; Product Version 10.2, June 2004, p. 290; available at <http://www.montana.edu/aolson/ee503/pspug.pdf> [accessed Sept. 27th, 2018]
- [32] AZoNetwork UK Ltd.; *Property Table: Titanium Dioxide - Titania (TiO₂)*; available at <https://www.azom.com/properties.aspx?ArticleID=1179> [accessed Sept. 27th, 2018]
- [33] Milo, Ron; Jorgensen, Paul; Moran, Uri; Weber, Griffin; Springer, Michael; *Sizes of various cells in BioNumbers - the database of key numbers in molecular and cell biology*; Nucleic Acids Res. 2010 Jan; 38(Database issue): D750–D753.; DOI: 10.1093/nar/gkp889.; available at <http://bionumbers.hms.harvard.edu/files/Sizes%20of%20various%20cells.pdf> [accessed Sept. 28th, 2018]